

1

Abstract

2

# Measurement of total hadronic cross sections in the LArIAT experiment

3

4

Elena Gramellini

5

2018

6

Abstract goes here. Limit 750 words.

7

8

9  
10  
11  
12  
13  
14

15

16

17

18



21

*A mia mamma e mio babbo,*

22

*grazie per le radici e grazie per le ali.*

23

*To my mom and dad,*

24

*thank you for the roots and thank you for the wings.*

# Contents

26	<b>Acknowledgements</b>	<b>vi</b>
27	<b>0 Data and MC preparation for the Cross Section Measurements</b>	<b>1</b>
28	0.1 Cross Section Analyses Data Sets . . . . .	1
29	0.2 Construction of a Monte Carlo Simulation for LArIAT . . . . .	3
30	0.2.1 G4Beamline . . . . .	3
31	0.2.2 Data Driven MC . . . . .	8
32	0.3 Estimate of Backgrounds in the Pion Cross Section . . . . .	11
33	0.3.1 Background from Pion Capture and Decay . . . . .	11
34	0.3.2 Contributions from the Beamline Background . . . . .	14
35	0.4 Estimate of Energy Loss before the TPC . . . . .	17
36	0.5 Tracking Studies . . . . .	21
37	0.5.1 Angular Resolution . . . . .	21
38	0.6 Calorimetry Studies . . . . .	27
39	0.6.1 Kinetic Energy Measurement . . . . .	27
40	<b>1 Negative Pion Cross Section Measurement</b>	<b>30</b>
41	1.1 Raw Cross Section . . . . .	30
42	1.1.1 Statistical Uncertainty . . . . .	32
43	1.1.2 Treatment of Systematics . . . . .	34
44	1.2 Corrections to the Raw Cross Section . . . . .	35

45	1.2.1	Background subtraction . . . . .	35
46	1.2.2	Efficiency Correction . . . . .	38
47	1.3	Results . . . . .	42
48	<b>2</b>	<b>Positive Kaon Cross Section Measurement</b>	<b>44</b>
49	2.1	Raw Cross Section . . . . .	44
50	2.2	Corrections to the Raw Cross Section . . . . .	47
51	2.3	Results . . . . .	48
52	2.4	Results . . . . .	48

# Acknowledgements

*“Dunque io ringrazio tutti quanti.*

*Specie la mia mamma che mi ha fatto così funky.”*

– Articolo 31, Tanqi Funky, 1996 –

*“At last, I thank everyone.*

*Especially my mom who made me so funky.”*

– Articolo 31, Tanqi Funky, 1996 –

A lot of people are awesome, especially you, since you probably agreed to read this when it was a draft.

# Chapter 0

## Data and MC preparation for the Cross Section Measurements

*“Il dolce non lo mangi mai, ma qualche volta ti rifai.*

*Abbracciami”*

– Pietro Ciampi, L’amore e’ tutto qui, 1971 –

This chapter describes the work done on the data and Monte Carlo samples in preparation for the cross section analyses. This entails the choice of the datasets and the production of the information needed to construct the Monte Carlo Simulation (Section 0.1), the construction and use of said Monte Carlo simulation (section 0.2), the study of backgrounds for the pion cross section (Section 0.3), the study of the energy loss between WC4 and TPC (Section 0.4), the study of the tracking in the TPC (Section 0.5), and study of the calorimetry response (Section 0.6).

### 0.1 Cross Section Analyses Data Sets

We choose LArIAT Run-II as the data period for the  $(\pi^-, \text{Ar})$  and  $(K^+, \text{Ar})$  total hadronic cross section analyses. Data taking for the this period started on 03/15/2016



78 and ended on 07/31/2016. Since we are interested in beamline and TPC information,  
 79 we ask basic requirements on the operational status of the time of flight, wire chambers  
 80 and TPC to form the good run list for this period, which we informally call “lovely  
 81 runs”.

82 The subset of lovely runs chosen for the  $(\pi^-, \text{Ar})$  total hadronic cross section  
 83 analysis includes only the -60A and -100A magnet configurations in negative polarity,  
 84 even if LArIAT explored several other beamline configurations during Run-II. The -  
 85 60A and -100A combined data set accounts for approximately 90% of the total Run-II  
 86 negative polarity runs. The choice of the main two beamline settings limits the need  
 87 for the production of many different MC sets and related corrections, still maintaining  
 88 a high number of events.

89 Similarly, the subset of lovely runs chosen for the  $(K^+, \text{Ar})$  total hadronic cross  
 90 section analysis includes only the +60A and +100A magnet configurations in positive  
 91 polarity. It should be noted that kaons are extremely rare in the +60A sample, thus  
 92 the data sample for the  $(K^+, \text{Ar})$  cross section after the mass selection is about 90%  
 93 +100A runs, as shown in Table 1.

94 For the first measurements in LArIAT that uses both beamline and TPC infor-  
 95 mation, we choose strict requirements on the reconstruction of the WC tracks, the  
 96 so-called “Picky Track” sample (see Section ??). This choice presents two advantages:  
 97 the uncertainty on the momentum reconstruction for the “Picky Tracks” sample is  
 98 smaller compared to the “High Yield” sample, and the comparison with the beam-  
 99 line MC results is straightforward. A possible future update and cross check of these  
 100 analysis would be the use of the High Yield sample, where the statistics is about three  
 101 times higher.

102 The breakdown of beamline events as a function of the magnets settings is shown  
 103 in Table 1. The choice of the data sets determines the production of beamline MC  
 104 and serves as basis for the production of Data Driven MC, as shown in the next

105 sections.

## 106 0.2 Construction of a Monte Carlo Simulation for 107 LArIAT

108 For the simulation of LArIAT events and for the simulation of the datasets' particle  
109 make up, we use a combination of two MC generators: the G4Beamline Monte Carlo  
110 and the Data Driven single particle Monte Carlo (DDMC). We use the G4Beamline  
111 MC to simulate the particle transportation in the beamline and calculate the particle  
112 composition of the beam just after the fourth Wire Chamber (WC4). In order to  
113 simulate the beamline particles after WC4 and in the TPC, we use the DDMC.

### 114 0.2.1 G4Beamline

115 G4Beamline simulates the beam collision with the LArIAT secondary target, the  
116 energy deposited by the particles in the LArIAT beamline detectors, and the action  
117 of the LArIAT magnets, effectively accounting for particle transportation through the  
118 beamline from the LArIAT target until “Big Disk”, a fictional, void detector located  
119 just before the LArIAT cryostat. At the moment of this writing, G4Beamline does  
120 not simulated the responses of the beamline detectors. It is possible to interrogate the  
121 truth level information of the simulated particles in several points of the geometry.  
122 In order to ease the handshake between G4Beamline and the DDMC, we ask for  
123 the beam composition just after WC4. Since LArIAT data are taken under different

	I = 60 A	I = 100 A	Total
Data Events after $\pi/\mu/e$ Mass Selection	67068	71413	138481
Data Events after $K$ Mass Selection	274	2563	2837

Table 1: Number of data events which fit the  $\pi/\mu/e$  or  $K$  mass hypothesis as a function of magnet settings.

beam conditions, we need to simulate separately the beam composition according to the magnets' settings and the secondary beam intensity with G4Beamline. For the pion cross section analysis the relevant beam conditions are secondary beam energy of 64 GeV, negative polarity magnet with current of 100 A and 60 A. For the kaon cross section analysis the relevant beam conditions is a secondary beam energy of 64 GeV, positive polarity magnet with current of 100 A.

### Beam Composition for Negative Pion Cross Section

Even if pions are by far the biggest beam component in negative polarity runs, the LArIAT tertiary beam is not a pure pion beam. While useful to discriminate between pions, kaons, and protons, the beamline detectors are not sensitive enough to discriminate among the lighter particles in the beam: electrons, muons and pions fall under the same mass hypothesis. Thus, we need to assess the contamination from beamline particles other than pions in the event selections used for the pion cross section analysis and correct for its effects. The first step of this process is assessing the percentage of electrons and muons in the  $\pi/\mu/e$  beamline candidates via the G4Beamline MC. Since the beamline composition is a function of the magnet settings, we simulate separately events for magnet current of -60A and -100A. Figure 1 shows the momentum predictions from G4Beamline overlaid with data for the 60A runs (left) and for the 100A runs (right). The predictions for electrons, muons and pions have been staggered and their sum is area normalized to data. Albeit not perfect, these plots show a reasonable agreement between the momentum shapes in data and MC. We attribute the difference in shape to a two approximations performed in the MC. Firstly, G4Beamline lacks the simulation of the WC efficiency which is momentum dependent and leads to enhance the number events in the center of the momentum distribution. Secondly, G4Beamline stop tracking pions and their products if they decay in after WC1; in data, pion decays in flight can still create a trigger

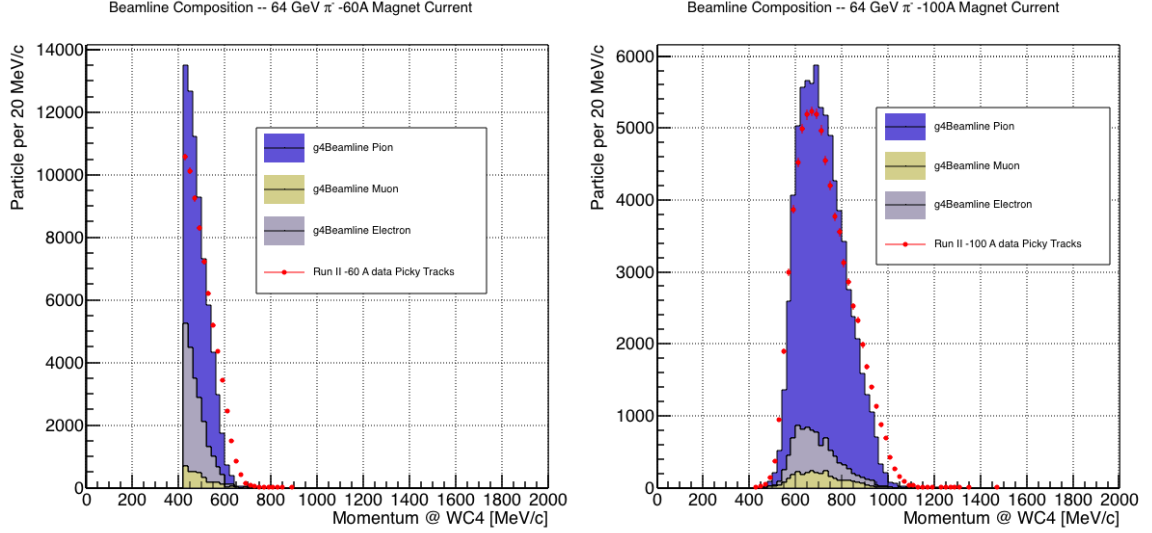


Figure 1: Beam composition for the -60A runs (left) and -100A runs (right). The solid blue plot represents the simulated pion content, the yellow plot represents the simulated muon content and the grey plot represents the simulated electron content. The plots are area normalized to the number of data events, shown in red.

	I = -60 A	I = -100 A
G4Pions	68.8 %	87.4 %
G4Muons	4.6 %	3.7 %
G4Electrons	26.6 %	8.9 %

Table 2: Simulated beamline composition per magnet settings

150 if the produced muon travels through the beamline detectors. In the pion cross sec-  
151 tion analysis, these differences between data and G4Beamline are accounted for as a  
152 systematic uncertainty related to the beam composition (see Section 1.2.1).

153 Table 2 shows the beam composition per magnet setting after the mass selection  
154 according to the G4Beamline simulation.

155 The estimated beam composition is used as a basis to estimate the background  
156 contamination in the  $(\pi^-, \text{Ar})$  cross section measurement, whose full treatment is  
157 described in section 0.3.

## 158 Beam Composition for Positive Kaon Cross Section

159 In the positive polarity runs, the tertiary beam composition is mainly pions and  
160 protons. The left side of Figure 2 shows the predictions for the momentum spectra  
161 for the 100A positive runs according to G4Beamline (solid colors) overlaid with data  
162 (black points). Since the LArIAT beamline detectors can discriminate between kaons  
163 and other particles, we do not rely on the G4Beamline simulation to estimate the  
164 beamline contamination in the pool of kaon candidates (as in the case of the pion  
165 cross section), but rather we use a data drive approach. The basic idea of this data  
166 driven approach is to estimate the bleed over from high and low mass peaks under  
167 the kaon peak by fitting the tails of the  $\pi/\mu/e$  and proton mass distributions, as  
168 shown in Figure 2 right side. Since the shape of the tails is unknown, the estimate  
169 is done multiple times varying the range and shape for reasonable functions. For  
170 example, to estimate the proton content under the kaon peak, we start by fitting the  
171 left tail of the proton mass distribution with a gaussian function between  $650 \text{ MeV}/c^2$   
172 and  $750 \text{ MeV}/c^2$ . We extend the fit function under the kaon peak and integrate the  
173 extended fit function between  $350\text{-}650 \text{ MeV}/c^2$ . We integrate the mass histogram  
174 in the same range and calculate the proton contamination as the ratio between the  
175 two integrals. We repeat this procedure for several fit shapes (gaussian, linear and  
176 exponential functions) and tail ranges. Finally, we calculate the contamination as  
177 the weighted average of single estimates, where the weights are calculated to be the  
178  $1./|1 - \chi^2|$  of the tail fits. The procedure is repeated for lighter particles mass peak  
179 independently. With 12 iterations of this method we find a proton contamination of  
180  $5.0 \pm 2.0 \%$  and a contamination from the lighter particles of  $0.2 \pm 0.5 \%$ . The  
181 estimate of the proton background is currently not used in the kaon cross section  
182 analysis, but it is a fundamental step to retrieve the true kaon cross section which  
183 will be implemented in the further development of the analysis.

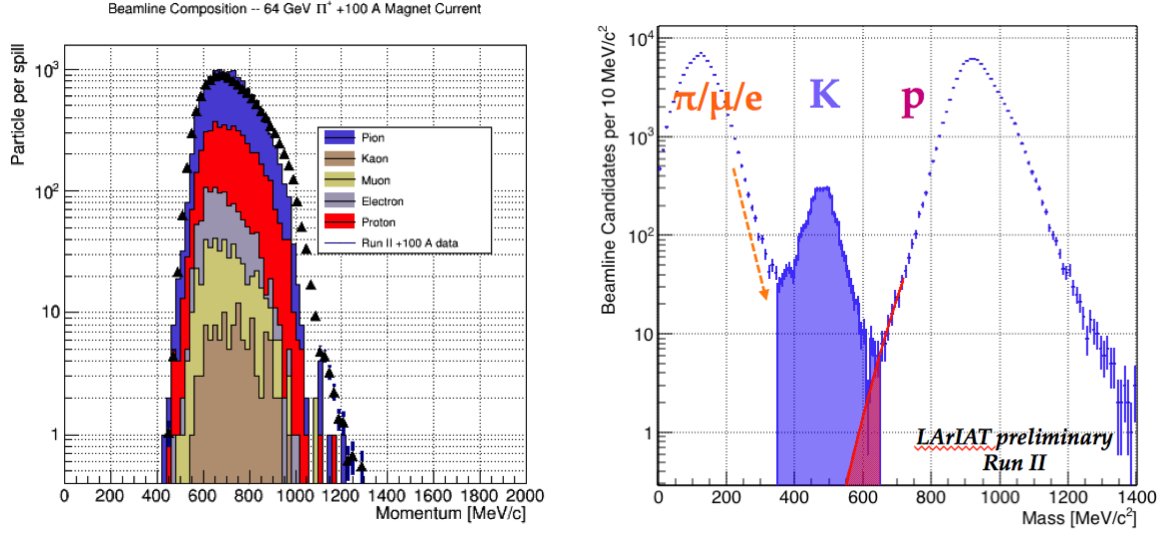


Figure 2: *Left*: Beam composition for the +100A runs after WC4 (no mass selection applied). The solid colors represent the contributions from the G4Beamline simulated particles: blue plot represents the simulated pion content, the yellow plot represents the simulated muon content and the grey plot represents the simulated positron content, the red the proton content and the mustard the kaon content. The plots are area normalized to the number of data events, shown in black. *Right*: Mass distribution for the Run-II positive runs, where the area under the kaon mass peak is highlighted in purple. The area under the extension of a possible fit for the proton tail is highlighted in red.

## 0.2.2 Data Driven MC

The Data Driven single particle Monte Carlo (DDMC) is a single particle gun which simulates the particle transportation from WC4 into the TPC leveraging on the beam-line data information. The DDMC uses the data momentum and position at WC4 to derive the event generation: a general sketch of the DDMC workflow is shown in Figure 3.

When producing a DDMC sample, beamline data from a particular running period and/or running condition are selected first. For example, data for the negative 60A runs and for the negative 100A runs inform the event generation stage of two different DDMC samples. Figure 4 schematically shows the data quantities of interest leveraged from data: the momentum  $(P_x, P_y, P_z)$  and position  $(X, Y)$  at WC4. For each data event, we obtain the particle position  $(X, Y)$  at WC4 directly from the data measurement; we calculate the components of the momentum using the beam-line measurement of the momentum magnitude in conjunction with the hits on WC3 and WC4 to determine the direction of the momentum vector, as described in section ???. The momentum and position of the selected data form a 5-dimensional tuple, which we sample thousands of times through a 5-dimensional hit-or-miss sampling procedure to generate the MC events. This sampling generates MC events with the same momentum and position distributions as data, with the additional benefit of accounting for the correlations between the  $P_x, P_y, P_z, X, Y$  variables. As an example, the results of the DDMC generation compared to data for the kaon +100A sample are shown in figure 5 for the  $P_z, X$  and  $Y$  distributions; as expected, MC and data agree within the statistical uncertainty by construction. A LArSoft simulation module then launches single particle MC from  $z = -100$  cm (the location of the WC4) using the generated events. The particles are free to decay and interact in their path from WC4 to the TPC according to the Geant4 simulation.

Using the DDMC technique ensures that the MC and data particles have very

211 similar momentum, position and angular distributions at WC4 and allows us to use  
 212 the MC sample in several occasions: to estimate the background contamination to  
 213 the pion cross section (see Section 0.3), to calibrate the energy loss upstream of the  
 214 TPC (see Section 0.4), or to study the tracking and the calorimetric performance  
 215 (sections 0.5 and 0.6). A small caveat is in order here: the DDMC is a single particle  
 216 Monte Carlo, which means that the beam pile-up is not simulated.

217 We generate six samples for the pion cross section measurement: three samples  
 218 of  $\sim 330000$  pions, muons and electrons to simulate the negative 60A runs, and three  
 219 samples of  $\sim 340000$  pions, muons and electrons for the negative 100A runs. We  
 220 generate a sample of 195000 kaons for the kaon cross section analysis.

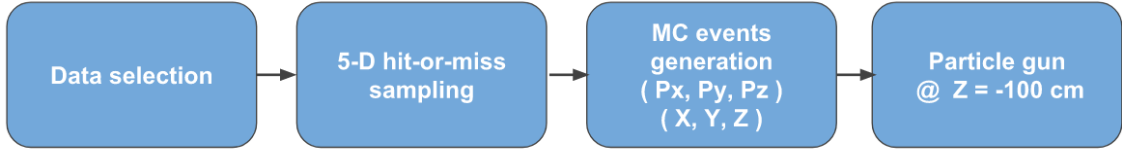


Figure 3: Workflow for Data Driven single particle Monte Carlo production.

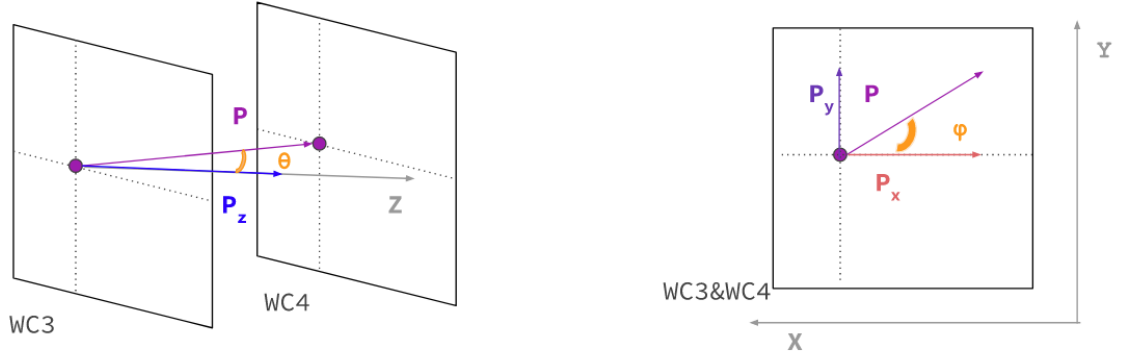


Figure 4: Scheme of the quantities of interest for the DDMC event generation:  $P_x, P_y, P_z, X, Y$  at WC4.



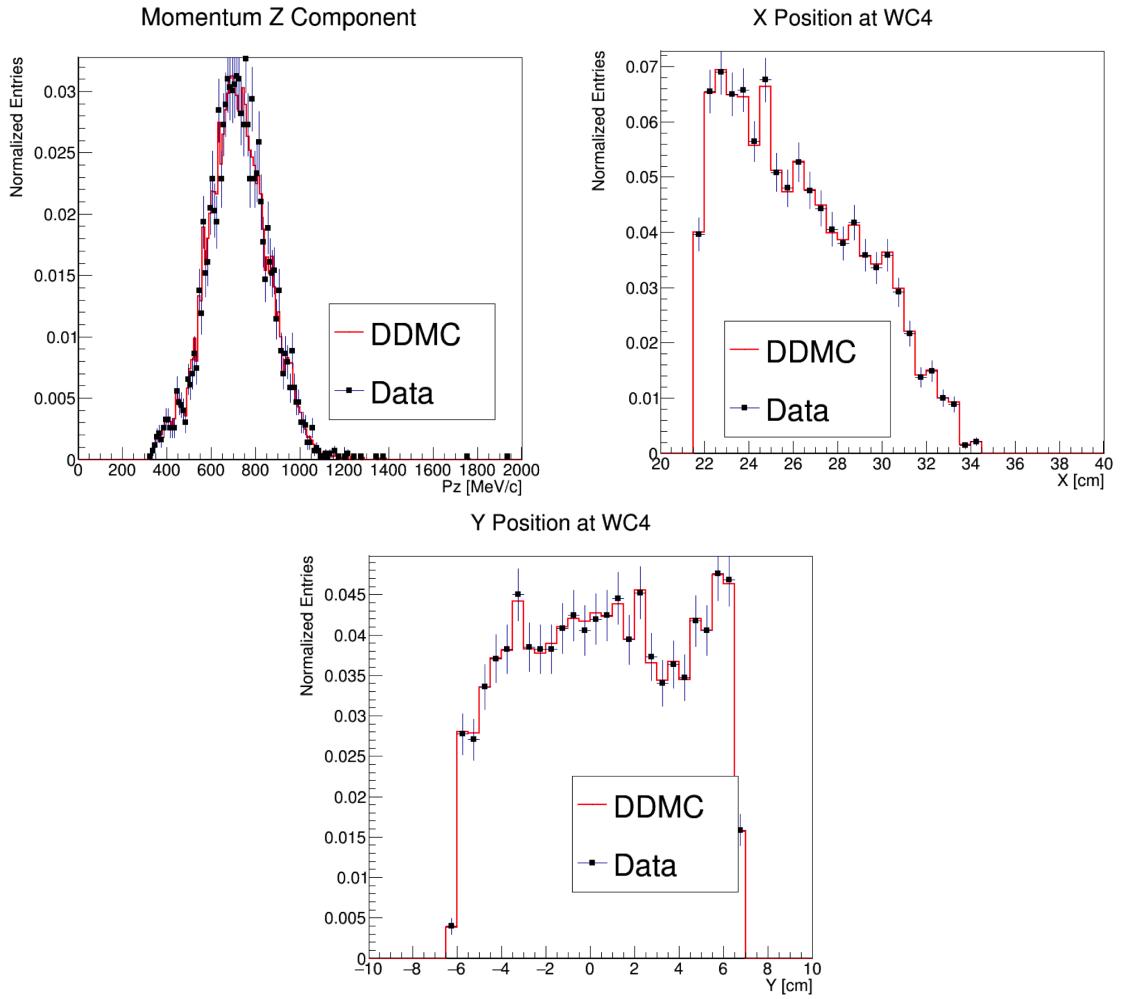


Figure 5: Comparison between generated quantities and data distributions for the 100A kaon sample: Z component of the momentum at WC4 (top left), X position at Wire Chamber 4 (top right), Y position at Wire Chamber 4 (bottom).

## 0.3 Estimate of Backgrounds in the Pion Cross Section

We use the beamline simulation and the DDMC simulation to estimate the background in the total hadronic pion cross section. Two categories of background exists for the negative pion cross section measurement: the one related to the pion interaction in the chamber, discussed in Section 0.3.1 and the one related to the beamline contamination, discussed in Section 0.3.2.

### 0.3.1 Background from Pion Capture and Decay

Our goal is to measure the total hadronic cross section for negative pions in argon. Since pion capture can be classified as an electromagnetic process and pion decay is a weak process, capture and decay represent unwanted interactions. We present here a study of capture and decay in Monte Carlo and the solution we adopted to mitigate their occurrence in the data sample.

For this MC study, we use a sample of MC pions generated according to the  $-60A$  beam profile with the DDMC (see Section 0.2.2). It is important to notice that capture occurs predominantly at rest, while decay may occur both in flight and at rest. Thus, we can highly mitigate capture and decay at rest by removing pions which would release all their energy in the TPC and stop. This translates into a momentum selection, where we keep only events whose WC momentum is above a certain threshold. Figure 6 shows the true momentum distribution for the primary pions<sup>1</sup> that arrive to the TPC (pink), that capture (green) or decay (blue) inside the TPC, on a linear scale (left) and on a log scale (right) vertical axis.

---

1. We use here the Geant4 denomination “primary” to indicate that the pion considered does not undergo interactions modifying its energy before getting to the TPC. In fact, not every pion shot from wire chamber four will arrive to the TPC as primary, some will decay or interact before the TPC.

243 In order to choose the selection value for the wire chamber momentum, it is  
 244 beneficial to estimate the ratio of events which capture or decay that survive the  
 245 selection in MC as a function of the momentum threshold, and compare it with the  
 246 survival ratio for all the 60A events. This is done in figure 7. We define the survival  
 247 ratio simply as the number of events surviving the true momentum selection divided  
 248 by the number of events of that category. We calculate the survival ratio separately  
 249 for the three event categories explained above: total (pink), capture (green) and decay  
 250 (blue). Selecting pions with momentum greater than 420 MeV/c reduces the capture  
 251 events by 99% while maintaining about 80% of the 60A data sample and almost the  
 252 entire 100A sample. Figure 8 shows the ratio of events which end their life in capture  
 253 (green) or decay (blue) over the total number of events as a function of the true  
 254 momentum at wire chamber four. This ratio is slightly dependent on the inelastic  
 255 cross section implemented in Geant4, as we are able to register a pion capture (or  
 256 decay) only if it did not interact inelastically in the TPC. We choose a momentum  
 257 threshold of 420 MeV/c because the percentage of capture events drops below 1% and  
 258 the percentage of decays is never above 2% for momenta greater than 420 MeV/c.  
 259 After the momentum selection, we evaluate the contribution of capture and decay to  
 260 be a negligibly small background to the cross section measurement compared to the  
 261 background related to the beamline which we will address in the next section.

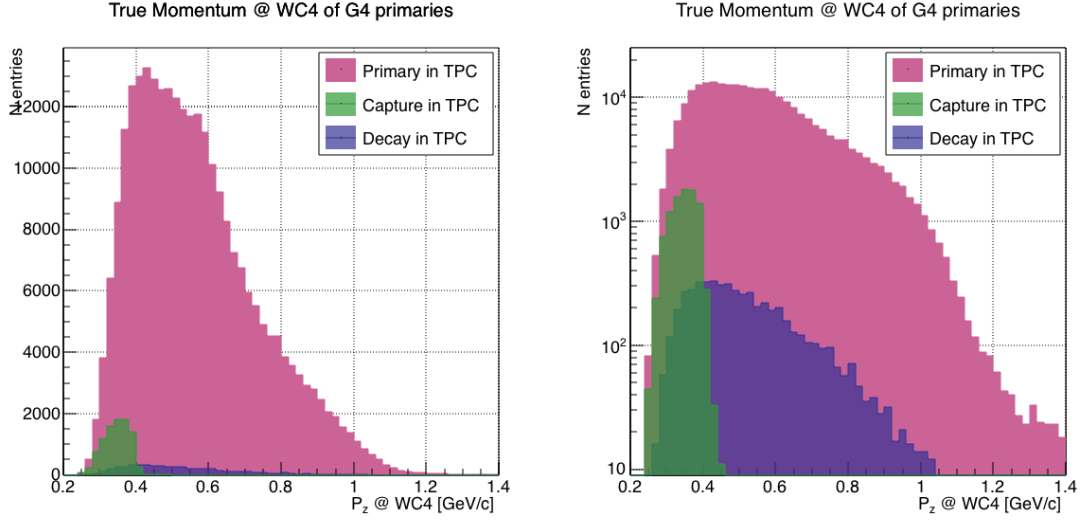


Figure 6: True momentum distribution at wire chamber 4 for every simulated pion arriving in the TPC (pink), ending its life in capture (green) or in decay (blue) in the TPC, linear vertical axis on the left, logarithmic on the right.

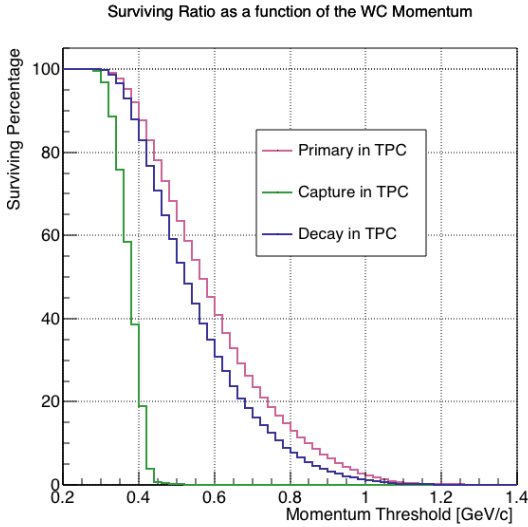


Figure 7: Survival ratio as a function of selection threshold on true momentum at wire chamber four for every simulated pion arriving in the TPC (pink), capture (green) or in decay (blue).

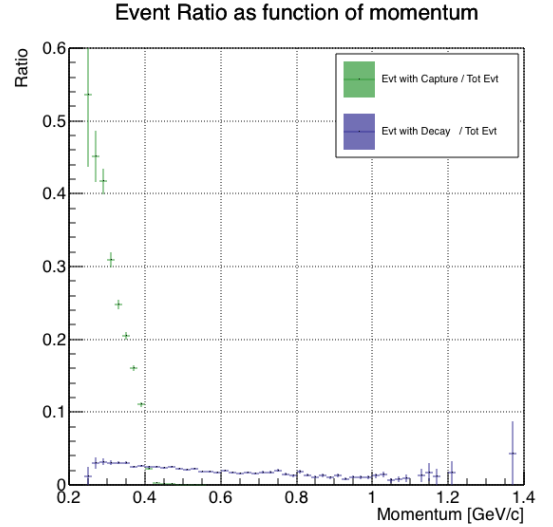


Figure 8: Ratio between the capture (green) and decay (blue) events over the total number of events as a function of the true momentum at wire chamber four.

### 0.3.2 Contributions from the Beamline Background

We define beamline background every TPC track matched to the WC track which is not a primary pion. Potentially, there are 4 different types of beamline background:

- 1) electrons,
- 2) muons,
- 3) secondaries from pion events,
- 4) matched pile up events.

The first step to quantify the effect of the beamline background on the pion cross section is to estimate what percentage of events used in the cross section calculation is not a primary pion. We start by noting that the last type of background, the “matched pile up” events, is a negligible fraction, because of the definition of the WC2TPC match: we deem the probability of a single match with a halo particle in the absence of a beamline particle<sup>2</sup> negligibly small. As shown in Section 0.2.1, we use G4Beamline to estimate the percentage of pions, muons and electrons at WC4, obtaining the composition shown in Table 2. The next step is to simulate those pions, muons and electrons from WC4 to the TPC with the DDMC and evaluate their contribution to the cross section. To do so, we start by simulating the same number of electrons, muons and pions with the DDMC and we apply the same selection chain (i.e. track multiplicity rejection, WC2TPC acceptance and shower rejection) on the three samples. The number of events per particle species surviving this selection is shown on table 3. In order to reproduce the closest make up of the beam to data, we weight each event of a given particle species according to the estimated beam composition. In case of 60A runs, for example, the weights are 0.688 for pions, 0.046 for muons and 0.266 for electrons.

---

2. Events with multiple WC2TPC matches are always rejected.

	Magnet Current -60A			Magnet Current -100 A		
	MC $\pi^-$	MC $\mu^-$	MC $e^-$	MC $\pi^-$	MC $\mu^-$	MC $e^-$
Total Initial events	334500	334500	334500	344500	344500	344500
After Multiplicity Rejection	330668	333420	198065	326576	344208	201380
After WC2TPC Selection	218239	296333	91139	230418	300228	98834
Evts After Shower Rejection	208063	288914	20293	219882	293585	17780
Selection Survival Rate	62.3%	86.6%	6.1%	63.8%	85.5%	5.2%
Beam Composition @WC4	68.8%	4.6 %	26.6 %	87.4 %	3.7 %	8.9 %
Beam Composition @TPC FF	88.5%	8.2%	3.3 %	94.0%	5.3%	0.7%

Table 3: MC selection flow per particle species.

286 It should be noted that pions may interact hadronically in the steel or in the  
 287 non-instrumented argon upstream to the TPC front face while travelling the length  
 288 of between WC4 and the TPC. Or, they could decay in flight between WC4 and the  
 289 TPC. One of the interaction products can leak into the TPC and be matched with the  
 290 WC track, contributing to the pool of events used for the cross section calculation. We  
 291 call this type of particles “secondaries” from pion events, with a terminology inspired  
 292 by Geant4. We estimate the number of secondaries using the DDMC pion sample.  
 293 The percentage of secondaries is given by the number of matched WC2TPC tracks  
 294 whose corresponding particle is not flagged as primary by Geant4. The secondary to  
 295 pion ratio is 4.9% in the 60A sample and 4.3% in the 100A sample.

296 We evaluate the beamline background contribution to the cross section by pro-  
 297 ducing the interacting and incident histograms for the events surviving the selection,  
 298 staggering the contributions for each particle species, as shown in Figure 9. From  
 299 those histograms, we are able to evaluate the contribution of pions and beamline  
 300 backgrounds to each bin of the interacting and incident histograms separately and  
 301 obtain the relative pion content. The relative pion content in each bin for the inter-  
 302 acting and incident histograms represents the correction applied to data. We take

here the interacting histogram as example, noting that the derivation of the correction for the incident histogram is identical. The number of entries in each bin of the interacting plot (Figure 9 left) is  $N_{\text{Int}}^{\text{TOT}}(E_i)$ , equal to the sum of the pions and beamline backgrounds in that bin, namely

$$N_{\text{Int}}^{\text{TOT}}(E_i) = N_{\text{Int}}^{\pi}(E_i) + \underbrace{N_{\text{Int}}^{\mu}(E_i) + N_{\text{Int}}^e(E_i) + N_{\text{Int}}^{\text{Secondary}}(E_i)}_{B_{\text{Int}}(E_i)}. \quad (1)$$

Thus, the relative pion content to each bin in MC can be calculated as follows

$$C_{\text{Int}}^{\pi MC}(E_i) = \frac{N_{\text{Int}}^{\pi MC}}{N_{\text{Int}}^{\text{TOTMC}}(E_i)} = \frac{N_{\text{Int}}^{\text{TOTMC}}(E_i) - B_{\text{Int}}^{\text{MC}}(E_i)}{N_{\text{Int}}^{\text{TOTMC}}(E_i)}. \quad (2)$$

In order to evaluate the pion content of each bin in data, we scale the measured bin by the corresponding relative pion content found in MC, as follows

$$N_{\text{Int}}^{\pi \text{RecoData}} = N_{\text{Int}}^{\text{TOTData}}(E_i) - B_{\text{Int}}^{\text{Data}}(E_i) = C_{\text{Int}}^{\pi MC}(E_i) N_{\text{Int}}^{\text{TOTData}}(E_i). \quad (3)$$

The pion content is evaluated separately in the interacting and incident histograms. Their ratio determines a correction to the measured raw cross section. For example, the measured raw cross section of a sample with enhanced muons content will tend to be lower than the raw cross section of a muon free sample. This is because most of the muons will cross the TPC without stopping, thus contributing almost exclusively to the incident histogram, forcing the pion content to be lower in the incident histogram than in the interacting; thus, the correction will tend to enhance the cross section.

## 0.4 Estimate of Energy Loss before the TPC

The beamline particles travel a path from where their momentum is measured in the beamline until they are tracked again inside the TPC. In the LArIAT geometry, a particle leaving the WC4 will encounter the materials listed in Table 4 before being registered again. The energy lost by the particle in this non-instrumented material modifies the particle's kinetic energy and directly affects the cross section measurement, as shown in equation ??.

Material	density [g/cm <sup>3</sup> ]	width [cm]
Fiberglass laminate (G10)	1.7	1.28
Liquid Argon	1.4	3.20
Stainless Steel	7.7	0.23
Titanium	4.5	0.04
Air	$1.2 \cdot 10^{-3}$	89.43
Plastic Scintillator	1.03	1.20 (+ 1.30)

Table 4: LArIAT material budget from WC4 to the TPC Front Face.

We derive an estimate of the energy loss between the beamline momentum measurement and the TPC ( $E_{loss}$ ) from the pion and kaon DDMC samples, since this quantity is not measurable directly on data. The  $E_{loss}$  distribution for the 60A and 100A pion sample is shown in figure 10, left and right respectively. The  $E_{loss}$  distribution for the whole kaon sample is shown in figure 11. A clear double peaked structure is visible, which is due to the particles either missing or hitting the HALO paddle: a schematic rendering of this occurrence is shown in figure 12. The kinematic at WC4 determines the trajectory of a particle and whether or not it will hit the halo paddle. In figure 13, we plot the true horizontal component of the momentum  $P_x$  versus the true  $X$  position at WC4 for pions missing the halo paddle (left) and for pions hitting the halo paddle (right) for the -60A MC simulation runs – analogous plots are obtained with the -100A pion simulation and with the kaon simulation. These distributions can be separated drawing a line in this position-momentum space. We



use a logistic regression [13] as a classifier to find the best separating line, shown in both plots as the red line. We classify as “hitting the halo paddle” all pions whose  $P_x$  and  $X$  are such that

$$P_x + 0.02 * X - 0.4 < 0$$

and as “missing the halo paddle” all pions whose  $P_x$  and  $X$  are such that

$$P_x + 0.02 * X - 0.4 > 0,$$

where the coefficients of the line are empirically found by the logistic regression estimation. Overall, this simple method classifies in the right category (hit or miss) about 86% of the pion events. In MC, we assign  $E_{loss} = 32 \pm 4$  MeV for pion events classified as “hitting the halo paddle”; we assign  $E_{loss} = 24 \pm 3$  MeV for pion events classified as “missing the halo paddle”. We apply the same classifier on data.

A scan of the simulated geometry showed an excess of 3 cm of uninstrumented argon compared with the surveyed detector geometry. We account for this difference by assigning in data  $E_{loss} = 24 \pm 6$  MeV for pion events classified as “hitting the halo paddle” and  $E_{loss} = 17 \pm 6$  MeV for pion events classified as “missing the halo paddle”, where the uncertainty is derived as the standard deviation of the double peaked distribution.

The summary of the values for used for  $E_{Loss}$  for the pion sample is listed in table 5 with the analogous results for the study on the kaon case.

	$E_{loss}$ [MeV]	
	Hitting Halo	Missing Halo
Pion MC	$32 \pm 4$	$24 \pm 3$
Pion Data	$25 \pm 6$	$17 \pm 6$
Kaon MC	$38 \pm 6$	$31 \pm 5$
Kaon Data	$26 \pm 7$	$22 \pm 7$

Table 5: Energy loss for pions and kaons.

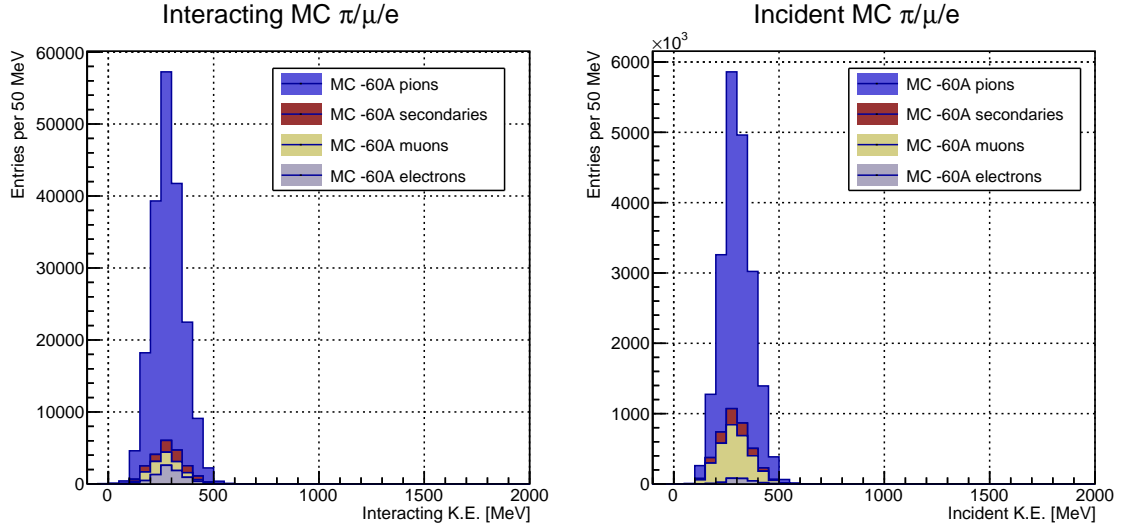


Figure 9: Left: staggered contributions to the interacting kinetic energy distribution for electron (grey), muons (yellow) and pion (blue) in the 60A simulation sample. Right: staggered contributions to the incident kinetic energy distribution for electron (grey), muons (yellow) and pion (blue) in the 60A simulation sample.

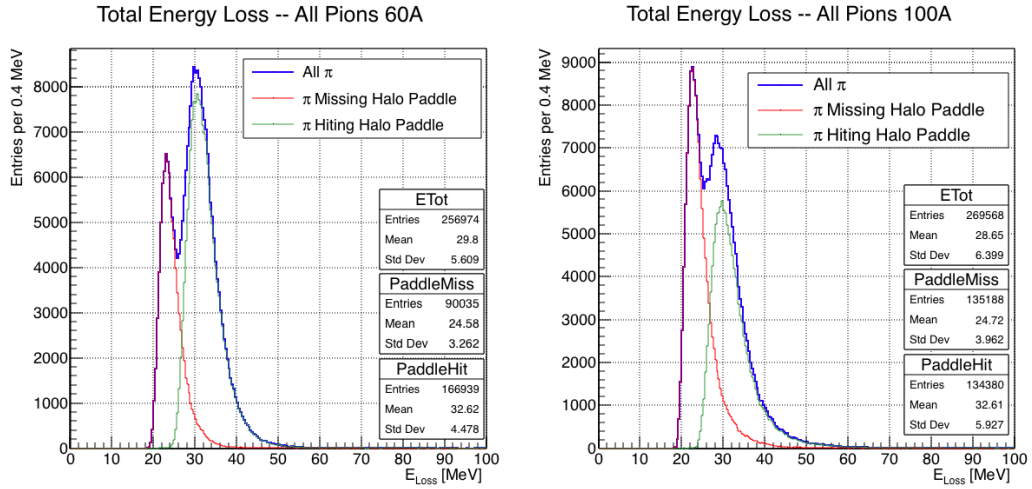


Figure 10: True energy loss between WC4 and the TPC front face according to the MC simulation of negative pions of the 60A runs (left) and of the 100A runs (right). The distribution for the whole data sample is shown in blue, the distribution for the pions missing the halo is shown in red, and the distribution for the pions hitting the halo is shown in green.

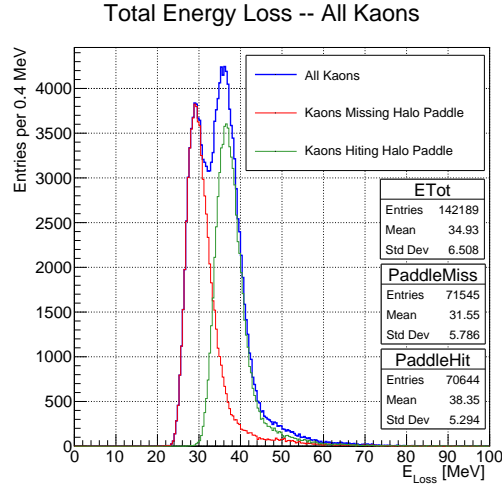


Figure 11: True energy loss between WC4 and the TPC front face according to the MC simulation of positive kaons in the 60A and 100A combined sample. The distribution for the whole data sample is shown in blue, the distribution for the kaons missing the halo is shown in red, and the distribution for the kaons hitting the halo is shown in green.

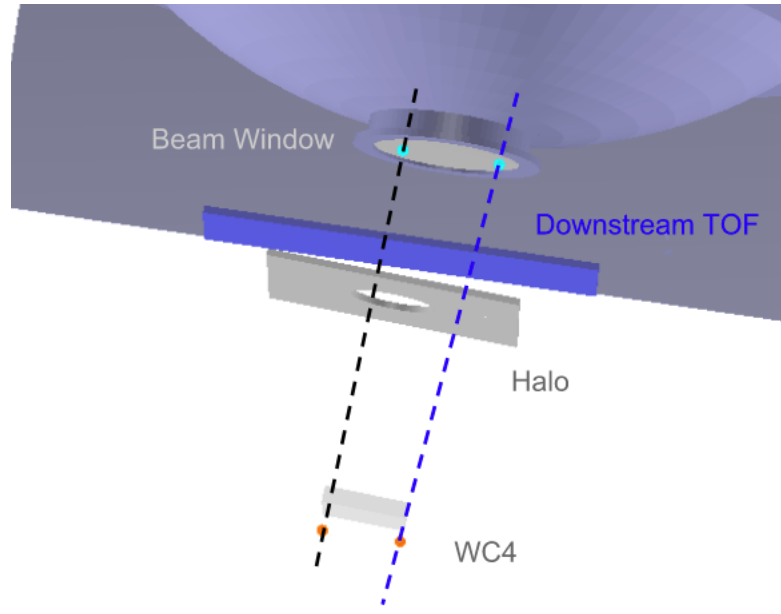


Figure 12: Schematic rendering of the particle path between WC4 and the TPC front face. The paddle with the hollow central circle represents the Halo paddle. We illustrate two possible trajectories: in black, a trajectory that miss the paddle and goes through the hole in the Halo, in blue a trajectory that hits the Halo paddle and goes through the scintillation material.

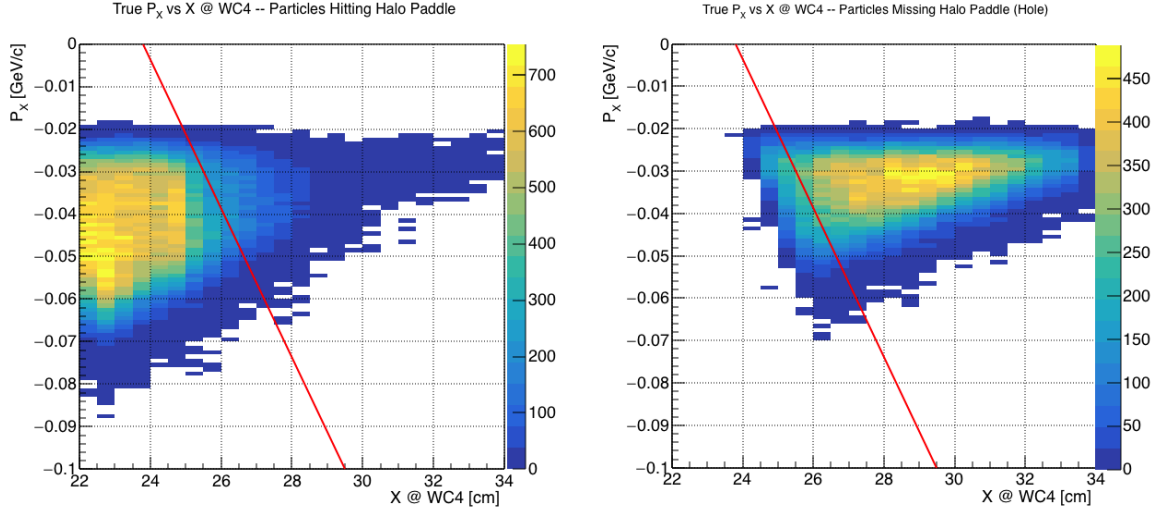


Figure 13: Horizontal component of the true momentum vs the horizontal position at WC4 for MC simulated pions of the 60A runs. The plot on the left shows the distribution for pion that miss the halo paddle and the plot on the right shows the distributions for pions that hit the halo. The form of the classifier is overlaid to both plots (red line).

## 0.5 Tracking Studies

The tracking of hadrons in the TPC determines both the beamline to TPC handshake and the identification of the interaction point within the TPC. Thus, it plays a fundamental role in the cross section measurements. We performed several studies geared towards the optimization of the package for tracking in the TPC. In particular, we studied a suitable set of parameters for the WC2TPC match and we optimized the clustering algorithm to maximize the efficiency of finding the interaction point on MC. Given the technical nature of these studies, we report them in Appendix ??.

We report here the evaluation of the angular resolution of the tracking algorithm in data and MC, due to its implication on the physics measurement.

### 0.5.1 Angular Resolution

Scope of this study is to understand and compare the tracking performances and angular resolution of the TPC tracking on data and MC. We use the angular resolution

of the tracking to determine the value of smallest angle that we can reconstruct with a non-zero efficiency, effectively determining a selection on the angular distribution of the cross section measurement due to the tracking performance.

We start by selecting all the WC2TPC matched tracks used for the cross section analysis. These tracks can contain from a minimum of 3 3D-space points to a maximum of 240 3D-space points. We fit a line to all the 3D-space points associated with the track. For each track we calculate the average distance between each point in space and the fit line as follows

$$\bar{d} = \frac{\sum_i^N d_i}{N}, \quad (4)$$

where  $N$  is the number of 3D-space points of the track and  $d_i$  is the distance of the  $i$ -th space point to the line fit. Several tests to compare the goodness of fit between data and MC have been considered. We decided to use  $\bar{d}$  for its straightforward interpretation. The  $\bar{d}$  distribution for data and MC is shown in Figure 16 for pions and in Figure 18 for kaons and shows a relatively good agreement between data and MC.

A visual representation of the procedure used to evaluate the angular resolution is shown in Figure 14. For each track, we order the space points according to their Z position along the positive beam direction (panel a) and we split them in two sets: the first set contains all the points belonging to the first half of the track and the second set contains all the points belonging the second half of the track. We remove the last four points in the first set and the first four points in the second set, so to have a gap in the middle of the original track (panel b). We fit the first and the second set of points with two lines (panel c). We then calculate the angle between the fit of the first and second half  $\alpha$  (panel d). The angle  $\alpha$  determines the spatial resolution of the tracking. The distributions for data and MC for  $\alpha$  are given in Figure 17 for pions and in Figure 19 for kaons. The mean of the data and MC angular resolution are reported in Table tab:AngRes for pions and kaons in data and MC.

Interaction angles smaller than the angle resolution are indistinguishable for the reconstruction. Therefore, we assess our ability to measure the cross section to be limited to interaction angles greater than 5.0 deg. More accurate studies of the angular resolution as a function of the kinetic energy and track length, albeit interesting, are left for an improvement of the analysis.

It is beneficial to take a moment to describe the definition of interaction angle. In case of elastic scattering, the definition is straightforward: the interaction angle is the angle between the incoming and outgoing hadron, i.e.

$$\theta = \cos^{-1} \left( \frac{\vec{p}_{\text{incoming}} \cdot \vec{p}_{\text{outgoing}}}{|\vec{p}_{\text{incoming}}| |\vec{p}_{\text{outgoing}}|} \right). \quad (5)$$

In case of inelastic scattering, the presence of several topologies requires a more complex definition, as shown in figure 15. We define the scattering angle as the biggest of the angles between the incoming hadron and the visible daughters, where the visible daughters are charged particles that travel more than 0.47 cm in the detector (see panel a); in case all the daughters are invisible, the angle is assigned to be 90 deg (see panel b). We chose this working definition of scattering angle for inelastic scattering keeping in mind how our tracking reconstruction works: the tracking will stop correctly non of the daughters are is visible in the detector and it is likely to stop correctly if multiple daughters form an interaction vertex. The only “dangerous” case is the production of one charged daughter plus neutrals, which we can study with this working definition of scattering angle (see panel c).

We can see the effects of the angular resolution on the cross section by plotting the true Geant4 cross section for interaction angles greater than a minimum interaction

	Data	MC
Pions	$\bar{\alpha}_{Data} = (5.0 \pm 4.5) \text{ deg}$	$\bar{\alpha}_{MC} = (4.5 \pm 3.9) \text{ deg}$
Kaons	$\bar{\alpha}_{Data} = (4.3 \pm 3.7) \text{ deg}$	$\bar{\alpha}_{MC} = (4.4 \pm 3.6) \text{ deg}$

Table 6: Angular resolution for Pion and Kaon tracking in both data and MC.

angle. Figure 20 shows the true Geant4 cross section for interaction angles greater  
 than 0 deg (green), 4.5 deg (red), 5.0 deg (blue) and 9.0 deg (yellow). A small 0.5 deg  
 systematic shift between the mean of the data and MC angular resolution is present.

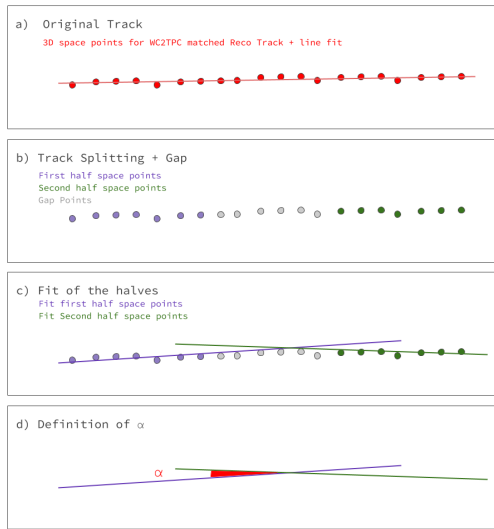


Figure 14: A visual representation of the procedure used to evaluate the angular resolution.

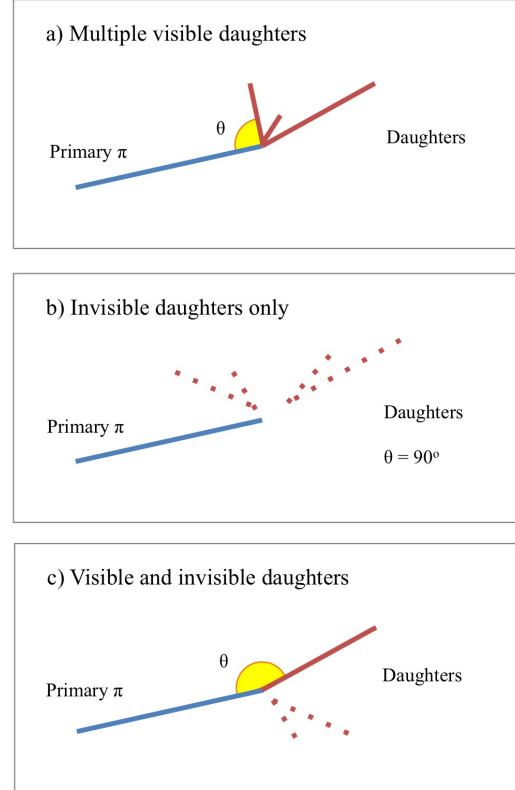


Figure 15: A visual representation of the scattering angle definition in case of inelastic scattering.

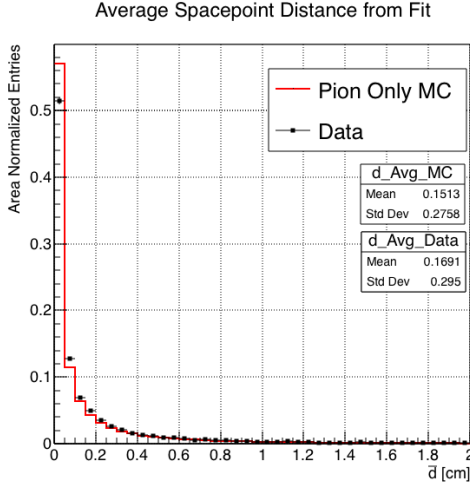


Figure 16: Distributions of the average distance between each 3D point in space and the fit line,  $\bar{d}$  for the data used in the pion cross section analysis and the pion only DDMC. The distributions are area normalized.

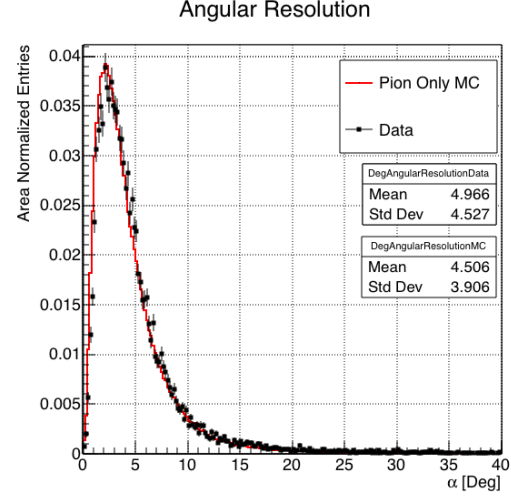


Figure 17: Distributions of angular resolution  $\alpha$  for data used in the pion cross section analysis and pion only DDMC. The distributions are area normalized.

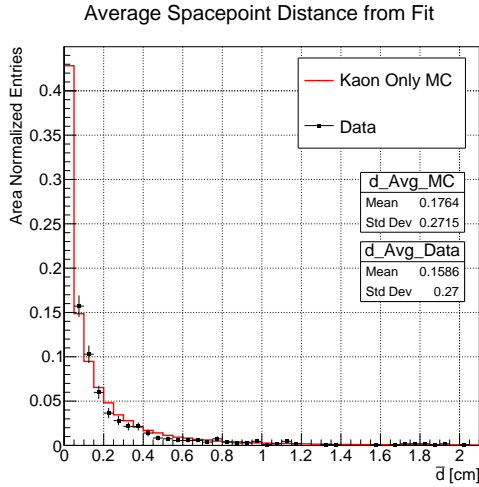


Figure 18: Distributions of the average distance between each 3D point in space and the fit line,  $\bar{d}$  for the data used in the kaon cross section analysis and the kaon only DDMC. The distributions are area normalized.

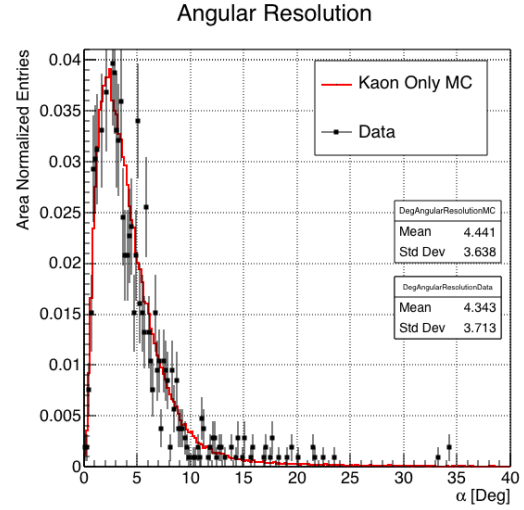


Figure 19: Distributions of angular resolution  $\alpha$  for data used in the kaon cross section analysis and kaon only DDMC. The distributions are area normalized.



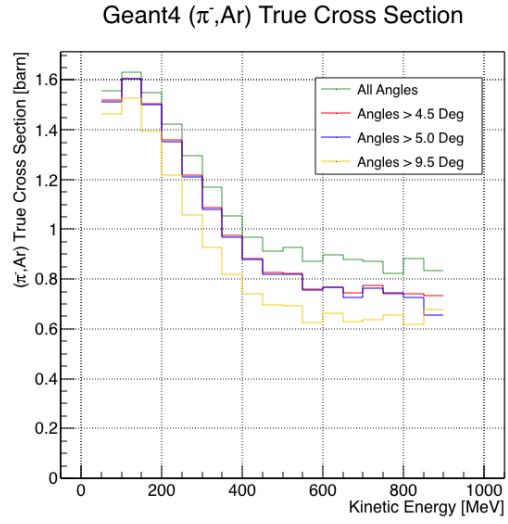


Figure 20: True ( $\pi^-$ , Ar) cross section for interaction angles greater than 0 deg (green), 4.5 deg (red), 5.0 deg (blue) and 9.0 deg (yellow).

## 0.6 Calorimetry Studies

The measured kinetic energy of a hadron candidate at each argon slab determines which bins of the interacting and incident histograms a selected event is going to fill. Thus, the energy measurement provided by the LArTPC is fundamental for the cross section analysis. In Appendix ??, we describe how we calibrate the TPC calorimetric response. In the following section, we describe how we measure the kinetic energy of the hadrons in the TPC.

### 0.6.1 Kinetic Energy Measurement

In this section, we define the measurement on the kinetic energy and determine the related uncertainty. We will propagate this uncertainty into the cross section measurement, as discussed in Section 1.1.2 for the pion cross section and in Section ?? for the kaon cross section.

The kinetic energy of a hadron at the  $j^{\text{th}}$  slice of argon in the TPC is given by

$$KE_j = \sqrt{p_{Beam}^2 + m_{Beam}^2} - m_{Beam} - E_{Loss} - E_{FF-j}, \quad (6)$$

where  $p_{Beam}$  is the momentum measured by the beamline detectors,  $m_{Beam}$  is the mass of the hadron as reported in the PDG,  $E_{Loss}$  is the energy loss between the beamline and the TPC, and  $E_{FF-j}$  is the energy that the hadron deposited from the TPC front face until the  $j^{\text{th}}$  slice. The uncertainty on  $KE_j$  is then given by

$$\delta KE_j = \sqrt{\delta p_{Beam}^2 + \delta E_{Loss}^2 + \delta E_{dep\ FF-j}^2}, \quad (7)$$

where we have dropped the uncertainty on the mass, since it is orders of magnitude smaller than the other uncertainties. We assume the relative uncertainty on  $p_{Beam}$  to be 2%, and the uncertainty on the energy loss upstream to be 7 MeV, as calculated

421 in Section 0.4. We describe the estimate of the uncertainty on  $E_{\text{FF-j}}$  in the rest of  
 422 this section.

423 The energy deposited by the hadron from the TPC front face until the  $j^{\text{th}}$  slice is  
 424 the sum of the measured energy deposited in each previous slabs  $E_i$ , i.e.

$$E_{\text{FF-j}} = \sum_{i < j} E_i, \quad (8)$$

425 where  $E_i$  is measured in each slab as the product of the stopping power,  $dE/dX_i$ ,  
 426 and the track pitch,  $Pitch_i$ , for that point. If we assume conservatively that the  
 427 measurements of  $E_i$  are not independent from one another, the uncertainty on  $E_{\text{FF-j}}$   
 428 becomes

$$\delta E_{\text{FF-j}} = (j - 1)\delta E_i, \quad (9)$$

429 where  $\delta E_i$  is the uncertainty on the energy loss in one slab of argon.

430 The left side of Figure 21 shows the distribution of the energy deposited in each  
 431 slab of argon, for the 60A negative pion dataset in black and for the pion only MC  
 432 in blue. The analogous plot for the -100A negative pion data set is show on the right  
 433 side of Figure 21. The distributions are fitted with a landau displayed in red for data  
 434 and in teal for MC. The uncertainty on  $E_i$  is given by the width of the Landau fit to  
 435 the data. A small systematic uncertainty is given by a 1.0% difference between the  
 436 most probable value of the landau fits in data and MC.

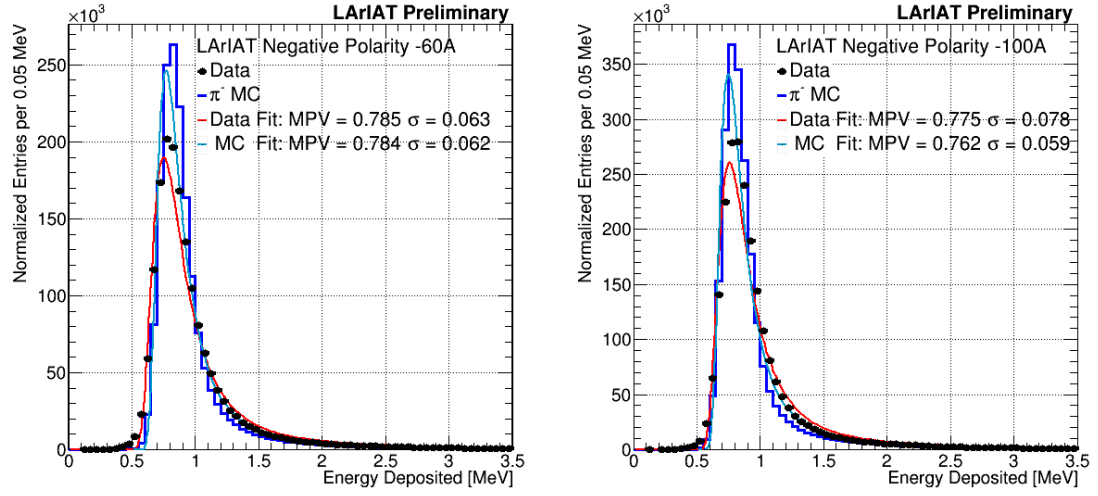


Figure 21: Energy deposited  $E_i$  in a single slab of argon for the pion -60A runs (left) and -100A runs (right). The data is shown in black, the MC in blue. The distributions are fitted with a landau displayed in red for data and in teal for MC.

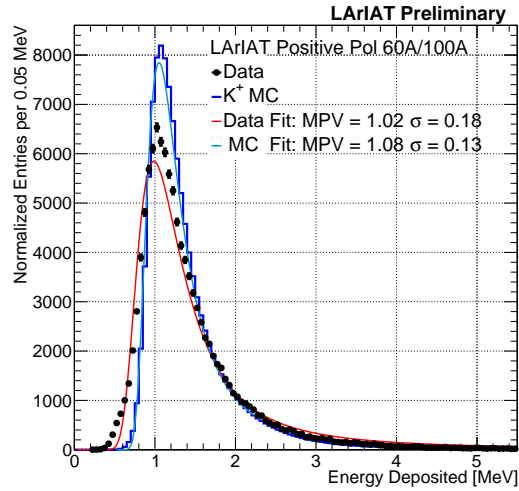


Figure 22: Energy deposited  $E_i$  in a single slab of argon for the kaons of the +60A runs and +100A runs. The data is shown in black, the MC in blue. The distributions are fitted with a landau displayed in red for data and in teal for MC.

# Chapter 1

## Negative Pion Cross Section Measurement

*“Y ella es flama que se eleva, Y es un pájaro a volar.  
En la noche que se incendia, estrella de oscuridad  
que busca entre la tiniebla, la dulce hoguera del beso.”*  
– Lila Downs, Benediction And Dream, 2002 –

In this chapter, we show the result of the thin slice method to measure the ( $\pi^-$ -Ar) total hadronic cross section. In Section 1.1, we start by measuring the raw cross section, i.e. the cross section obtained exclusively using data reconstruction, without any additional corrections. In Section 1.2, we apply a statistical subtraction of the background contributions based on simulation and a correction for detection inefficiency. The final results are presented in Section 1.3.

### 1.1 Raw Cross Section

We measure the raw ( $\pi^-$ -Ar) total hadronic cross section as a function of the kinetic energy in the two chosen data sets, the -60A and -100A negative runs. As we will

clarify in Section 1.2, the corrections to the raw cross section depend on the beam conditions and need to be calculated independently for the two datasets. Thus, we present here the measurement of the raw cross section on the two datasets separately.

As stated in section ??, the raw cross section is given by the equation ??

$$\sigma_{TOT}(E_i) = \frac{1}{n\delta X} \frac{N_{Int}^{TOT}(E_i)}{N_{Inc}^{TOT}(E_i)}, \quad (1.1)$$

where  $N_{Int}^{TOT}$  is the measured number of particles interacting at kinetic energy  $E_i$ ,  $N_{Inc}^{TOT}$  is the measured number of particles incident on an argon slice at kinetic energy  $E_i$ ,  $n$  is the density of the target centers and  $\delta X$  is the thickness of the argon slice. The density of the target centers and the slab thickness are  $n = 0.021 \cdot 10^{24} \text{ cm}^{-3}$  and  $\delta X = 0.47 \text{ cm}$ , respectively.

Figure 1.1 shows the distribution of  $N_{Int}^{TOT}$  as a function of the kinetic energy for the 60A dataset on the left and for the 100A dataset on the right. The data central points are represented by black dots, the statistical uncertainty is shown in black, while the systematic uncertainty is shown in red. Data is displayed over the  $N_{Int}^{TOT}$  distribution obtained with a MC mixed sample of pions, muon and electrons (additional details on the composition will be provided in Section ??). The contribution from the simulated pions is shown in blue, the one from secondaries in red, the one from muons in yellow and the ones from electrons in gray. The simulated pion's and backgrounds' contributions are stacked; the sum of the integrals from each particle species is normalized to the integral of the data.

Figure 1.2 shows the distribution of  $N_{Inc}^{TOT}$  for the 60A dataset on the left and for the 100A dataset on the right. Data is displayed over the MC. The same color scheme and normalization procedure is used for both the interacting and incident histograms.

Figure 1.3 shows the raw cross section for the 60A dataset on the left and for the 100A dataset on the right, statistical uncertainty in black and systematic uncertainty

477 in red. The raw data cross section is overlaid to the reconstructed cross section for  
 478 the MC mixed sample, displayed in azure. Since the background contributions and  
 479 the detector effects for the 60A and 100A sample are different, it is premature to  
 480 compare the raw cross sections obtained from the two samples at this point.

481 We describe the calculation of the statistical uncertainty for the interacting, in-  
 482 cident and cross section distributions in Section 1.1.1; we describe the procedure to  
 483 calculate the corresponding systematics uncertainty on Section 1.1.2.

### 484 1.1.1 Statistical Uncertainty

485 The statistical uncertainty for a given kinetic energy bin of the cross section is cal-  
 486 culated by error propagation from the statistical uncertainty on  $N_{\text{Inc}}^{\text{TOT}}$  and  $N_{\text{Int}}^{\text{TOT}}$   
 487 correspondent bin. Since the number of incident particles in each energy bin is given  
 488 by a simple counting, we assume that  $N_{\text{Inc}}^{\text{TOT}}$  is distributed as a poissonian with mean  
 489 and variance equal to  $N_{\text{Inc}}^{\text{TOT}}$  in each bin. On the other hand,  $N_{\text{Int}}^{\text{TOT}}$  follows a bino-  
 490 mial distribution: a particle in a given energy bin might or might not interact. The  
 491 variance for the binomial is given by

$$\text{Var}[N_{\text{Int}}^{\text{TOT}}] = \mathcal{N} P_{\text{Interacting}} (1 - P_{\text{Interacting}}). \quad (1.2)$$

492 Since the interaction probability  $P_{\text{Interacting}}$  is  $\frac{N_{\text{Int}}^{\text{TOT}}}{N_{\text{Inc}}^{\text{TOT}}}$  and the number of tries  $\mathcal{N}$  is  
 493  $N_{\text{Inc}}^{\text{TOT}}$ , equation 1.2 translates into

$$\text{Var}[N_{\text{Int}}^{\text{TOT}}] = N_{\text{Inc}}^{\text{TOT}} \frac{N_{\text{Int}}^{\text{TOT}}}{N_{\text{Inc}}^{\text{TOT}}} (1 - \frac{N_{\text{Int}}^{\text{TOT}}}{N_{\text{Inc}}^{\text{TOT}}}) = N_{\text{Int}}^{\text{TOT}} (1 - \frac{N_{\text{Int}}^{\text{TOT}}}{N_{\text{Inc}}^{\text{TOT}}}). \quad (1.3)$$

494  $N_{\text{Inc}}^{\text{TOT}}$  and  $N_{\text{Int}}^{\text{TOT}}$  are not independent. The statistical uncertainty on the cross  
 495 section is thus calculated as

$$\delta\sigma_{\text{TOT}}(E) = \sigma_{\text{TOT}}(E) \left( \frac{\delta N_{\text{Int}}^{\text{TOT}}}{N_{\text{Int}}^{\text{TOT}}} + \frac{\delta N_{\text{Inc}}^{\text{TOT}}}{N_{\text{Inc}}^{\text{TOT}}} \right) \quad (1.4)$$

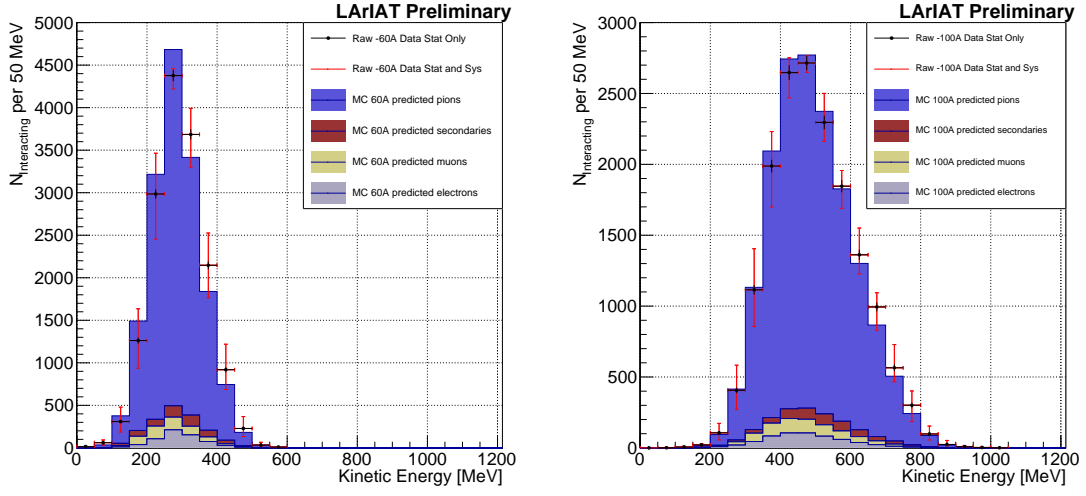


Figure 1.1: Raw number of interacting pion candidates as a function of the reconstructed kinetic energy for the 60A runs (left) and for the 100A runs (right). The statistical uncertainties are shown in black, the systematic uncertainties in red.

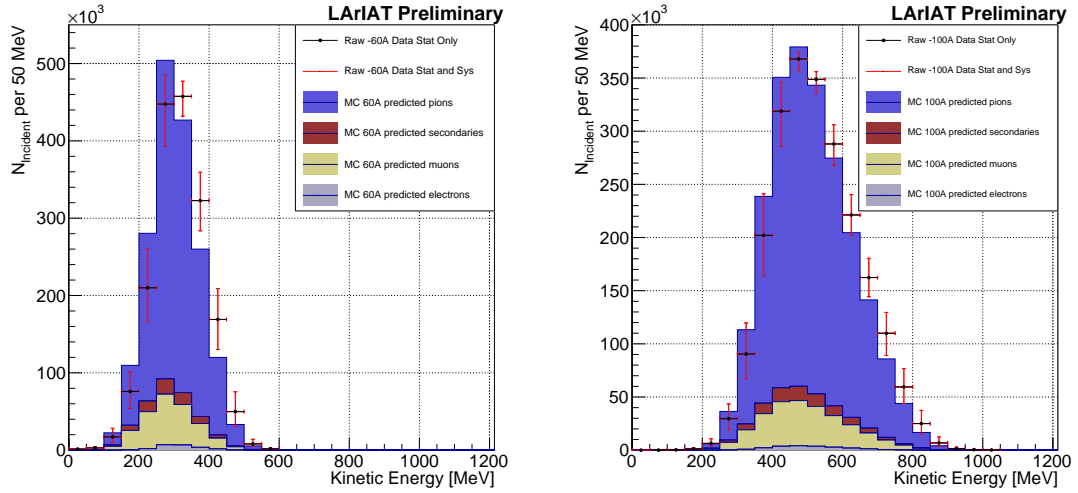


Figure 1.2: Raw number of incident pion candidates as a function of the reconstructed kinetic energy for the 60A runs (left) and for the 100A runs (right). The statistical uncertainty is shown in black, the systematic uncertainties in red.



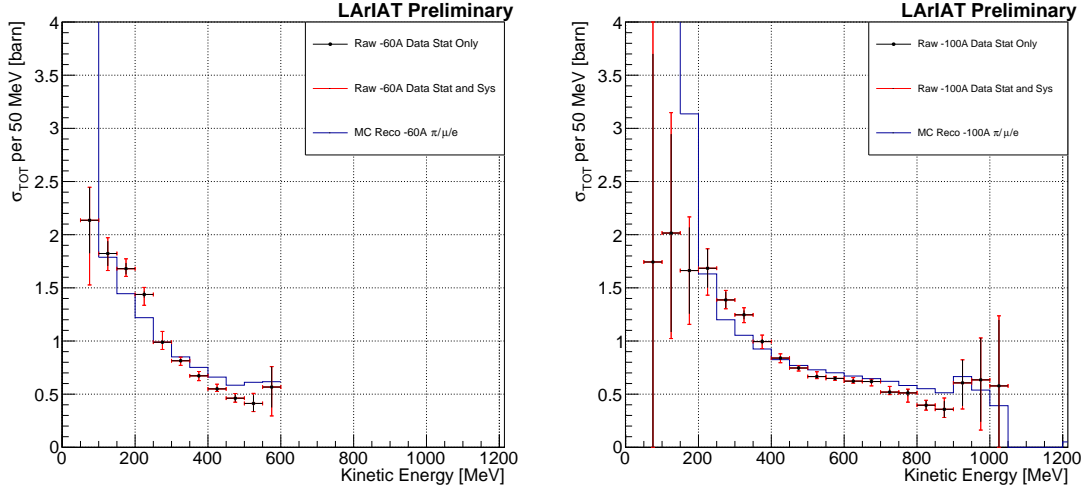


Figure 1.3: Raw ( $\pi^-$ -Ar) total hadronic cross section for the 60A runs (left) and for the 100A runs (right). The statistical uncertainty is shown in black, the systematic uncertainties in red. The raw cross section obtained with a MC mixed sample of pions, muon and electrons in the percentage predicted by G4Beamline is shown in azure.

496 where:

$$\delta N_{\text{Inc}}^{\text{TOT}} = \sqrt{N_{\text{Inc}}^{\text{TOT}}} \quad (1.5)$$

$$\delta N_{\text{Int}}^{\text{TOT}} = \sqrt{N_{\text{Int}}^{\text{TOT}} \left( 1 - \frac{N_{\text{Int}}^{\text{TOT}}}{N_{\text{Inc}}^{\text{TOT}}} \right)}. \quad (1.6)$$

## 497 1.1.2 Treatment of Systematics

498 The only systematic effect considered in the measurement of the raw cross section  
 499 results from the propagation of the uncertainty associate with the measurement of  
 500 the kinetic energy at each argon slab. As shown in Section 0.6.1, the uncertainty on  
 501 the kinetic energy of a pion candidate at the  $j^{\text{th}}$  slab of argon is given by

$$\delta KE_j = \sqrt{\delta p_{\text{Beam}}^2 + \delta E_{\text{Loss}}^2 + \delta E_{\text{dep FF-j}}^2} \quad (1.7)$$

$$= \sqrt{(2\% p_{\text{Beam}})^2 + (6 \text{ [MeV]})^2 + (j-1)^2 (\sim 0.08 \text{ [MeV]})^2}. \quad (1.8)$$

502 We propagate this uncertainty by varying the energy measurement  $KE_j$  at each  
 503 argon slab. We measure  $N_{\text{Inc}}^{\text{TOT}}$ ,  $N_{\text{Int}}^{\text{TOT}}$  and the cross section in three cases: first  
 504 assigning the measured  $KE_j$  at each kinetic energy sampling, then assigning  $KE_j +$   
 505  $\delta KE_j$ , and finally assigning  $KE_j - \delta KE_j$ . The difference between the values obtained  
 506 using the  $KE_j$  sampling and the maximum and minimum values in each kinetic energy  
 507 bin determines the systematic uncertainty.

## 508 1.2 Corrections to the Raw Cross Section

509 As described in section ??, we need to apply a background correction and an efficiency  
 510 correction in order to derive the true pion cross section from the raw cross section.  
 511 The true cross section is given in equation ??,

$$\sigma_{TOT}^{\pi^-}(E_i) = \frac{1}{n\delta X} \frac{\epsilon^{\text{Inc}}(E_i)}{\epsilon^{\text{Int}}(E_i)} \frac{C_{\text{Int}}^{\pi MC}(E_i)}{C_{\text{Inc}}^{\pi MC}(E_i)} \frac{N_{\text{Int}}^{\text{TOT}}(E_i)}{N_{\text{Inc}}^{\text{TOT}}(E_i)}. \quad (??)$$

512 Section 1.2.1 describes the evaluation of pion content in the interacting and inci-  
 513 dent histograms, ( $C_{\text{Int}}^{\pi MC}(E_i)$  and  $C_{\text{Inc}}^{\pi MC}(E_i)$ ) and the propagation to the cross section  
 514 measurement of the relative systematic uncertainties.

515 Section 1.2.2 describes the procedure employed to obtain the efficiency corrections  
 516  $\epsilon^{\text{Int}}(E_i)$  and  $\epsilon^{\text{Inc}}(E_i)$  and the propagation to the cross section measurement of the  
 517 relative uncertainties.

### 518 1.2.1 Background subtraction

519 We use the procedure described in 0.3.2 to evaluate the relative pion content in  
 520 the interacting histogram  $C_{\text{Int}}^{\pi MC}(E_i)$  and the relative pion content in the incident  
 521  $C_{\text{Inc}}^{\pi MC}(E_i)$ . We start by evaluating the relative pion content assuming the beamline  
 522 composition simulated by G4Beamline, whose pion, muon and electron percentages  
 523 per beam condition are reported again in the first line of Table 1.1. The left side of

Figure 1.4 shows the MC estimated relative pion content for the interacting histogram as function of kinetic energy for the 60A runs (top) and 100A runs (bottom). The right side of the same figure shows the MC estimated relative pion content for the incident histogram as function of kinetic energy for the 60A runs (top) and 100A runs (bottom). In Figure 1.4 the central curves displayed in light blue are obtained using the beamline composition as predicted by G4Beamline: these are the correction curves for the relative pion content applied to data.

So, the question now becomes: how well do we know the beamline composition? In absence of additional data constraints, we take a 100% systematic uncertainty on the electron content, reported in lines 3 and 4 of Table 1.1. The effect of doubling or halving the electron percentage in the beam on the pion relative content is displayed in red in Figure 1.4. We reserve a slightly different treatment for the muon content. Since G4Beamline tracks only particles which cross all the wire chambers, pion events that decay in flight from WC1 to WC4 are not recorded by G4Beamline. Pion decays in the beamline could be trigger the beamline detectors in data, if the produced muon proceeds in the beamline. Thus, we take the G4Beamline prediction for muons as a lower bound in the composition: the effect of doubling the muon content (line 2 in Table 1.1) is shown in blue on Figure 1.4. A future study of data from additional beamline detectors such as the Aerogel Chernkov detectors [42] or the muon range stack (see Section ??) has the potential of a narrowing the systematics uncertainty coming from the beamline composition.

We propagate the uncertainty on the beamline composition as a systematic uncertainty to the cross section by varying the beam composition for all the cases listed in Table 1.1 and evaluating variation of obtained data cross sections in each bin. This systematic uncertainty is summed in quadrature with the statistical uncertainty and the systematic uncertainty related to the kinetic energy measurement.

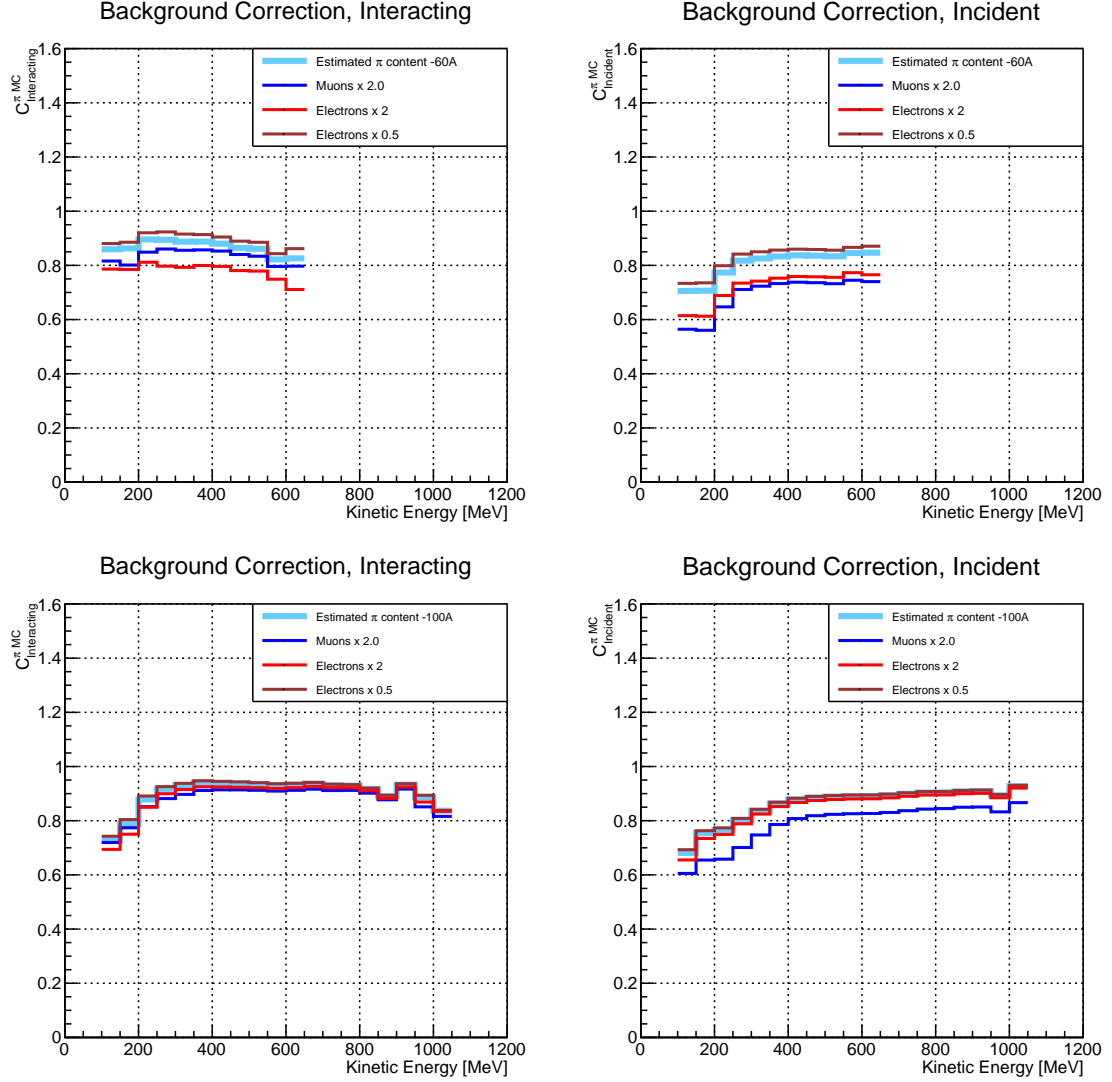


Figure 1.4: *Left:* MC estimated relative pion content for interacting histogram a function of kinetic energy for the 60A runs (top) and 100A runs (bottom), predicted background content in azure and muon and electron content variation in blue and red. *Right:* MC estimated relative pion content for incident histogram a function of kinetic energy for the 60A runs (top) and 100A (bottom), predicted background content in azure and muon and electron content variation in blue and red

### 1.2.2 Efficiency Correction

The interaction point for a track used in the total hadronic cross section analysis is defined to be the last point of the WC2TPC matched track which lies inside the fiducial volume. This definition is independent from the topology of the interaction. If the TPC track stops within the fiducial volume, its last point will be the interaction point, no matter what the products of the interaction look like; if the track crosses the boundaries of the fiducial volume, the track will be considered “through going” and no interaction point will be found. Given this definition, it is evident that we rely on the tracking algorithm to discern where the interaction occurred in the TPC and correctly stop the tracking. The tracking algorithm has an intrinsic angle resolution as shown in section 0.5.1, which limits its efficiency, especially in the case of elastic scattering occurring at low angles. Thus, we need to apply an efficiency correction to data in order to retrieve the true cross section. The efficiency correction is evaluated separately for the interacting and incident histograms, namely  $\epsilon_i^{\text{int}}$  and  $\epsilon_i^{\text{inc}}$ , and propagated to the cross section as shown in equation ??.

#### Efficiency Correction: Procedure

We describe here the procedure to calculate the efficiency correction taking the interacting histogram as example and noting that the procedure is identical for the incident histogram.

We derive the correction on a set of pure pion MC, calculating its value bin by bin as the ratio between the true bin content and the correspondent reconstructed bin content. The correction is then applied to the relevant bin in data. In formulae, the efficiency correction is calculated to be

$$\epsilon^{\text{Int}}(E_i) = \frac{N_{\text{Interacting}}^{\pi \text{ Reco MC}}(E_i)}{N_{\text{Interacting}}^{\pi \text{ True MC}}(E_i)}, \quad (1.9)$$

where  $N_{\text{Int}}^{\pi \text{ True MC}}(E_i)$  is the content of the  $i$ -th bin in for the true interacting histogram, and  $N_{\text{Int}}^{\pi \text{ Reco MC}}(E_i)$  is the content of the  $i$ -th bin in for the reconstructed interacting histogram. The correction is applied to data as follows

$$N_{\text{Int}}^{\pi \text{ True Data}}(E_i) = \frac{N_{\text{Int}}^{\pi \text{ Reco Data}}(E_i)}{\epsilon^{\text{Int}}(E_i)} = N_{\text{Int}}^{\pi \text{ Reco Data}}(E_i) \frac{N_{\text{Int}}^{\pi \text{ True MC}}(E_i)}{N_{\text{Int}}^{\pi \text{ Reco MC}}(E_i)}. \quad (1.10)$$

where  $N_{\text{Int}}^{\pi \text{ Reco Data}}(E_i)$  is the background subtracted bin content of the  $i$ -th bin in for the reconstructed interacting histogram for data, i.e.

$$N_{\text{Int}}^{\pi \text{ Reco Data}}(E_i) = N_{\text{Int}}^{\text{TOT Data}}(E_i) - B_{\text{Int}}^{\text{Data}}(E_i) = C_{\text{Int}}^{\pi \text{ MC}}(E_i) N_{\text{Int}}^{\text{TOT Data}}(E_i). \quad (1.11)$$

In section 0.5.1, we estimated the angular resolution for data and MC to be  $\bar{\alpha}_{\text{Data}} = (5.0 \pm 4.5)$  deg and  $\bar{\alpha}_{\text{MC}} = (4.5 \pm 3.9)$  deg, respectively. Most interaction angles smaller than the angular resolution will thus be indistinguishable for the reconstruction. Thus, we claim we are able to measure the cross section for interaction angles greater than 5.0 deg. Geant4 simulates interactions at all angles, as shown in figure 1.7. In order to calculate the efficiency correction, we select events which have an interaction angle greater than a given  $\alpha_{\text{res}}$  to construct the true interacting and incident histograms (the denominator of the efficiency correction). The systematics on the efficiency correction is estimated by varying the value of  $\alpha_{\text{res}}$  between 0 deg and 4.5 deg and propagating the uncertainty on the cross section.

Figure 1.5 shows  $\epsilon^{\text{Int}}(E_i)$  in the left side and  $\epsilon^{\text{Inc}}(E_i)$  on the right as a function of the kinetic energy for the 60A runs and their systematic uncertainty. Similarly, figure 1.6 shows  $\epsilon^{\text{Int}}(E_i)$  in the left side and  $\epsilon^{\text{Inc}}(E_i)$  on the right as a function of the kinetic energy for the 100A runs and their systematic uncertainty.

	Magnet Current -60A			Magnet Current -100 A		
	MC $\pi^-$	MC $\mu^-$	MC $e^-$	MC $\pi^-$	MC $\mu^-$	MC $e^-$
Expected Composition	68.8 %	4.6 %	26.6 %	87.4 %	3.7 %	8.9 %
Composition 2x Muons	64.2 %	9.2 %	26.6 %	83.7 %	7.4 %	8.9 %
Composition 2x Electrons	42.2 %	4.6 %	53.2 %	78.5 %	3.7 %	17.8 %
Composition 0.5x Electrons	82.1 %	4.6 %	13.3 %	91.9 %	3.7 %	4.4 %

Table 1.1: Beam composition variation for the study of systematics due to beam contamination.

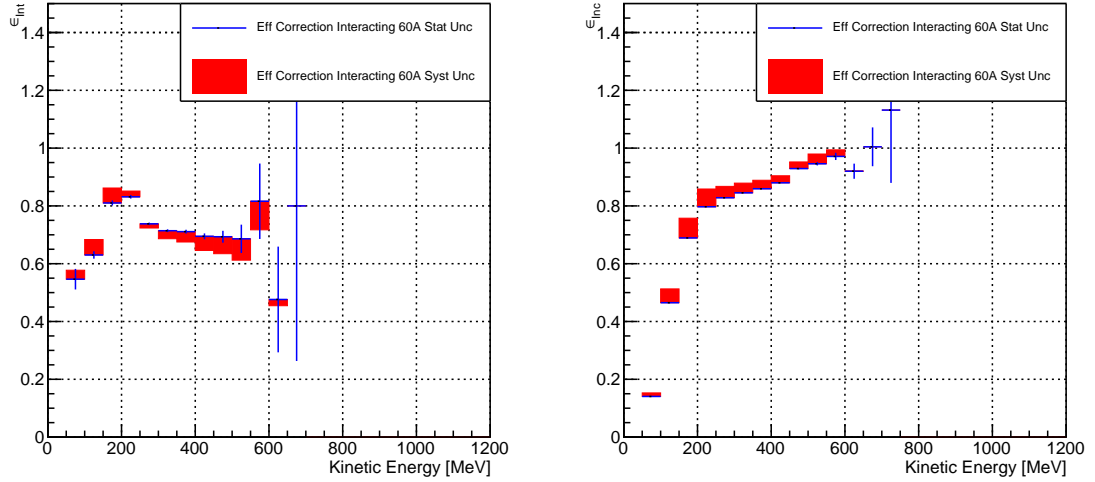


Figure 1.5: *Left*: Efficiency correction on the 60A interacting histogram, statistical uncertainty in blue, systematic uncertainty in red. *Right*: Efficiency correction on the 60A incident histogram, statistical uncertainty in blue, systematic uncertainty in red.

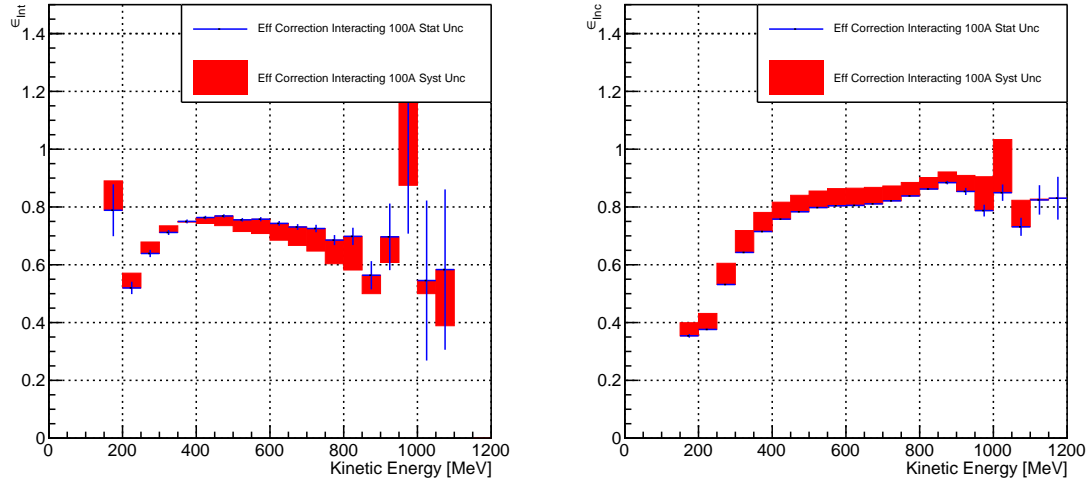


Figure 1.6: *Left*: Efficiency correction on the 100A interacting histogram, statistical uncertainty in blue, systematic uncertainty in red. *Right*: Efficiency correction on the 100A incident histogram, statistical uncertainty in blue, systematic uncertainty in red.

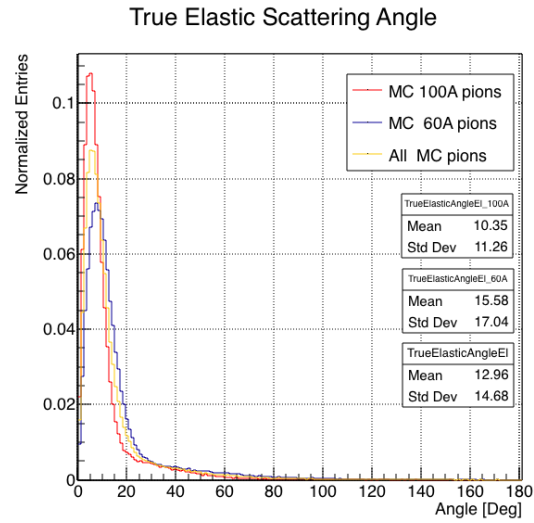


Figure 1.7: Distribution of the true scattering angle for a pion elastic scattering off the argon nucleus as simulated by Geant4.



## 1.3 Results

Figure 1.8 show the measurement of the ( $\pi^-$ -Ar) total hadronic cross section for scattering angles greater than  $5^\circ$ , as the result of the background subtraction and efficiency correction to the raw cross section. The top left plot is the measurement obtained on the 60A data, statistical uncertainty in black and systematic uncertainty in red. The top right plot is the measurement obtained on the 100A data, statistical uncertainty in black and systematic uncertainty in blue. The bottom plot shows the two measurements overlaid. In all three plot, the Geant4 prediction for the total hadronic cross section for angle scattering greater than  $5^\circ$  is displayed in green.

The systematic uncertainty on the cross section is the sum in quadrature of the statistical uncertainty, the systematic uncertainty related to the kinetic energy measurement, the systematic uncertainty related to the beam composition and the systematic uncertainty related to the efficiency correction.

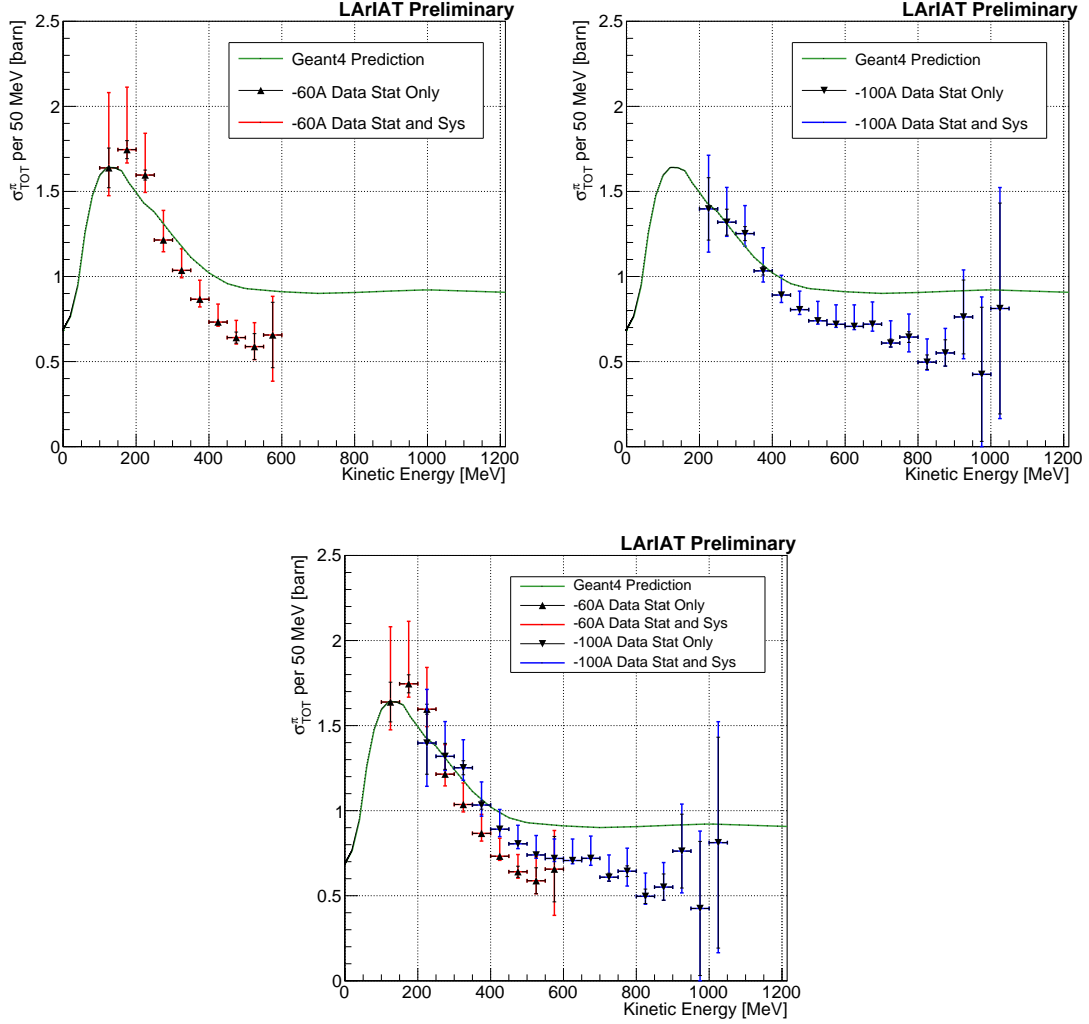


Figure 1.8: *Top Left:* ( $\pi^-$ -Ar) total hadronic cross section for scattering angles greater than  $5^\circ$  measured in the 60A sample, statistical uncertainty in black and systematic uncertainty in red. The Geant4 prediction for the total hadronic cross section for angle scattering greater than  $5^\circ$  is displayed in green.

*Top Right:* ( $\pi^-$ -Ar) total hadronic cross section for scattering angles greater than  $5^\circ$  measured in the 100A sample, statistical uncertainty in black and systematic uncertainty in blue. The Geant4 prediction for the total hadronic cross section for angle scattering greater than  $5^\circ$  is displayed in green.

*Bottom:* ( $\pi^-$ -Ar) total hadronic cross section measurements in the 60A and 100A samples overlaid with the Geant4 prediction (green).

## Chapter 2

# Positive Kaon Cross Section Measurement

In this chapter, we show the result of the thin slice method to measure the ( $K^+$ -Ar) total hadronic cross section. In Section 2.1, we start by measuring the raw cross section. In Section 2.2, we apply a statistical subtraction of the background contributions based on simulation and a correction for detection inefficiency. The final results are presented in Section 2.4.

### 2.1 Raw Cross Section

We measure the raw ( $K^+$ -Ar) total hadronic cross section as a function of the kinetic energy in the combined +60A and +100A dataset.

Similar to the pion case, the raw cross section is given by the equation ??

$$\sigma_{TOT}(E_i) = \frac{1}{n\delta X} \frac{N_{\text{Int}}^{\text{TOT}}(E_i)}{N_{\text{Inc}}^{\text{TOT}}(E_i)}, \quad (2.1)$$

where  $N_{\text{Int}}^{\text{TOT}}$  is the measured number of particles interacting at kinetic energy  $E_i$ ,  $N_{\text{Inc}}^{\text{TOT}}$  is the measured number of particles incident on an argon slice at kinetic energy

619  $E_i$ ,  $n$  is the density of the target centers and  $\delta X$  is the thickness of the argon slice.  
620 The density of the target centers and the slab thickness are  $n = 0.021 \cdot 10^{24} \text{ cm}^{-3}$  and  
621  $\delta X = 0.47 \text{ cm}$ , respectively.

622 As in the case of pions, kaons might decay or interact between WC4 and the TPC  
623 front face. Some of the interaction products may be wrongly matched to the WC  
624 track, forming the “secondary” particle’s background in the kaon sample. We estimate  
625 the effect of the contamination of secondaries through the DDMC kaon sample. Figure  
626 2.1 shows the distribution of  $N_{\text{Int}}^{\text{TOT}}$  as a function of the kinetic energy. The data  
627 central points are represented by black dots, the statistical uncertainty is shown in  
628 black, while the systematic uncertainty is shown in red. Data is displayed over the  
629  $N_{\text{Int}}^{\text{TOT}}$  distribution obtained with a DDMC sample of kaons shot from WC4. The  
630 contribution from the simulated kaons which interact hadronically is shown in pink,  
631 the contributions from kaon decay is shown in orange and the one from secondaries  
632 in red. The simulated kaon’s and secondaries’ contributions are stacked; the sum of  
633 their integrals is normalized to the integral of the data.

634 Figure 2.2 shows the distribution of  $N_{\text{Inc}}^{\text{TOT}}$ . Data is displayed over the MC. For the  
635  $N_{\text{Inc}}^{\text{TOT}}$  distribution we do not make a distinction between kaons that decay or interact  
636 hadronically because any kaon independently from its final interaction contributes  
637 to the flux of incident particles at given kinetic energy. The same normalization  
638 procedure is used for both the interacting and incident histograms.

639 Figure 2.3 shows the raw cross section, statistical uncertainty in black and system-  
640 atic uncertainty in red. The raw data cross section is overlaid to the reconstructed  
641 cross section for the MC mixed sample, displayed in azure. We calculate the sta-  
642 tistical uncertainty for the interacting, incident and cross section distributions in a  
643 similar fashion to the pion case as described in Section 1.1.1.

644 As in the pion case, the only systematic effect considered in the measurement of  
645 the raw cross section results from the propagation of the uncertainty associate with

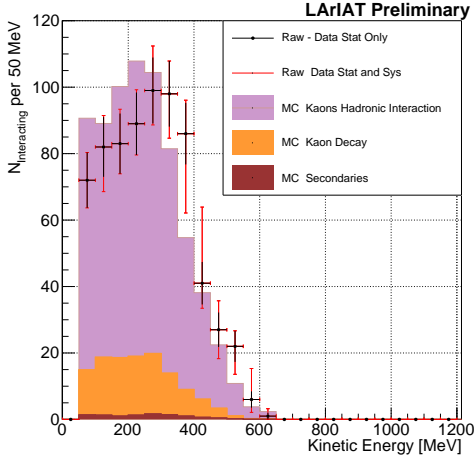


Figure 2.1: Raw number of interacting kaon candidates as a function of the reconstructed kinetic energy. The statistical uncertainties are shown in black, the systematic uncertainties in red.

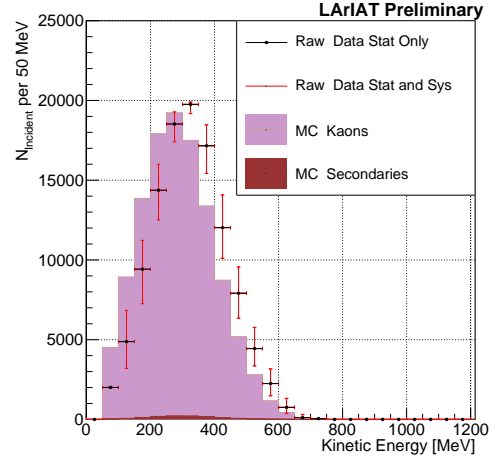


Figure 2.2: Raw number of incident kaon candidates as a function of the reconstructed kinetic energy. The statistical uncertainty is shown in black, the systematic uncertainties in red.

646 the measurement of the kinetic energy at each argon slab. For kaons, the uncertainty  
 647 on the kinetic energy of a candidate at the  $j^{th}$  slab of argon is given by

$$\delta KE_j = \sqrt{\delta p_{Beam}^2 + \delta E_{Loss}^2 + \delta E_{dep\ FF-j}^2} \quad (2.2)$$

$$= \sqrt{(2\% p_{Beam})^2 + (7 \text{ [MeV]})^2 + (j - 1)^2 (\sim 0.18 \text{ [MeV]})^2}. \quad (2.3)$$

648 We propagate this uncertainty by varying the energy measurement  $KE_j$  at each  
 649 argon slab. We measure  $N_{Inc}^{TOT}$ ,  $N_{Int}^{TOT}$  and the cross section in three cases: first  
 650 assigning the measured  $KE_j$  at each kinetic energy sampling, then assigning  $KE_j +$   
 651  $\delta KE_j$ , and finally assigning  $KE_j - \delta KE_j$ . The difference between the values obtained  
 652 using the  $KE_j$  sampling and the maximum and minimum values in each kinetic energy  
 653 bin determines the systematic uncertainty.

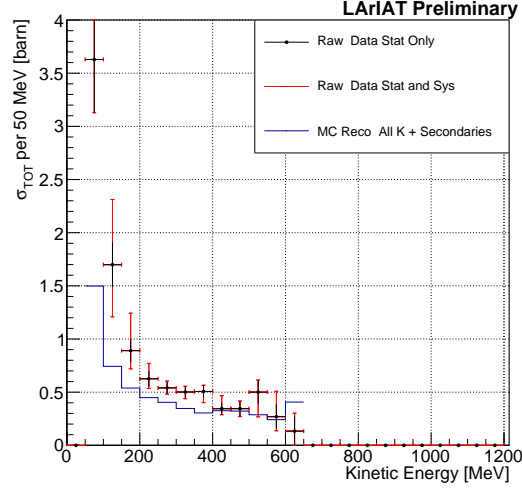


Figure 2.3: Raw ( $K^+$ -Ar) total hadronic cross section. The statistical uncertainty is shown in black, the systematic uncertainties in red. The raw cross section obtained with a MC sample of kaons is shown in azure. For the MC cross section, we include the contributions from secondaries.

## 2.2 Corrections to the Raw Cross Section

As described in section ??, we need to apply a background correction and an efficiency correction in order to derive the true Kaon cross section from the raw cross section. The true cross section is given in equation ??,

$$\sigma_{TOT}^{K^+}(E_i) = \frac{1}{n\delta X} \frac{\epsilon^{\text{Inc}}(E_i)}{\epsilon^{\text{Int}}(E_i)} \frac{C_{\text{Int}}^{KMC}(E_i)}{C_{\text{Inc}}^{KMC}(E_i)} \frac{N_{\text{Int}}^{\text{TOT}}(E_i)}{N_{\text{Inc}}^{\text{TOT}}(E_i)}. \quad (??)$$

Currently, the only background considered for the kaon hadronic cross section comes from the presence of secondaries. A further development of the analysis will need to account for the presence of a small proton contamination. Figure 2.4 shows the relative kaon content for the interacting and incident histograms.

As described in 1.2.2 for the pion case, we derive the correction on a set of pure kaon MC, calculating its value bin by bin as the ratio between the true bin content and the correspondent reconstructed bin content. The correction is then applied to the relevant bin in data. The efficiency correction is evaluated separately for the

interacting and incident histograms, namely  $\epsilon_i^{\text{int}}$  and  $\epsilon_i^{\text{inc}}$ , and propagated to the cross section as shown in equation ??.

In section 0.5.1, we estimated the angular resolution for data and MC to be  $\bar{\alpha}_{Data} = (4.3 \pm 3.7)$  deg and  $\bar{\alpha}_{MC} = (4.4 \pm 3.6)$  deg, respectively. Most interaction angles smaller than the angular resolution will thus be indistinguishable for the reconstruction. Thus, we claim we are able to measure the cross section for interaction angles greater than 4.5 deg. Geant4 simulates interactions at all angles: in order to calculate the efficiency correction, we select events which have an interaction angle greater than a  $\alpha_{res}$  to construct the true interacting and incident histograms (the denominator of the efficiency correction). The systematics on the efficiency correction is estimated by varying the value of  $\alpha_{res}$  between 0 deg and 4.5 deg and propagating the uncertainty on the cross section.

Figure 2.5 shows  $\epsilon^{\text{Int}}(E_i)$  in the left side and  $\epsilon^{\text{Inc}}(E_i)$  on the right as a function of the kinetic energy for the kaon sample and their systematic uncertainty.

## 2.3 Results

## 2.4 Results

Figure 2.6 show the measurement of the ( $K^+$ -Ar) total hadronic cross section for scattering angles greater than  $5^\circ$ , as the result of the background subtraction and efficiency correction to the raw cross section. The plot shows the measurement obtained on the full dataset, statistical uncertainty in black and systematic uncertainty in red. The Geant4 prediction for the total hadronic cross section for angle scattering greater than  $5^\circ$  is displayed in green.

The systematic uncertainty on the cross section is the sum in quadrature of the statistical uncertainty, the systematic uncertainty related to the kinetic energy mea-

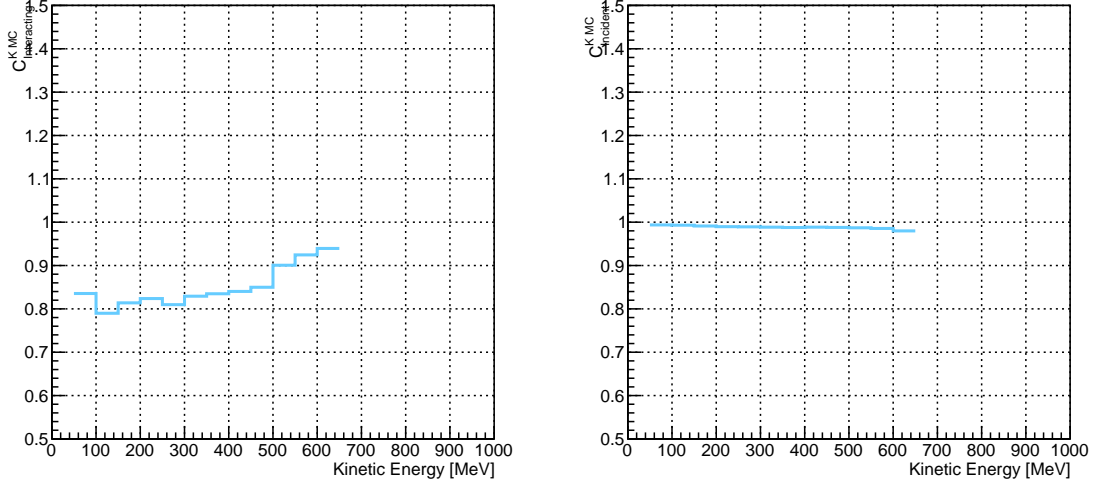


Figure 2.4: *Left*: MC estimated relative kaon content for kaons interacting hadronically as function of kinetic energy. *Right*: MC estimated relative kaon content for incident histogram a function of kinetic energy.

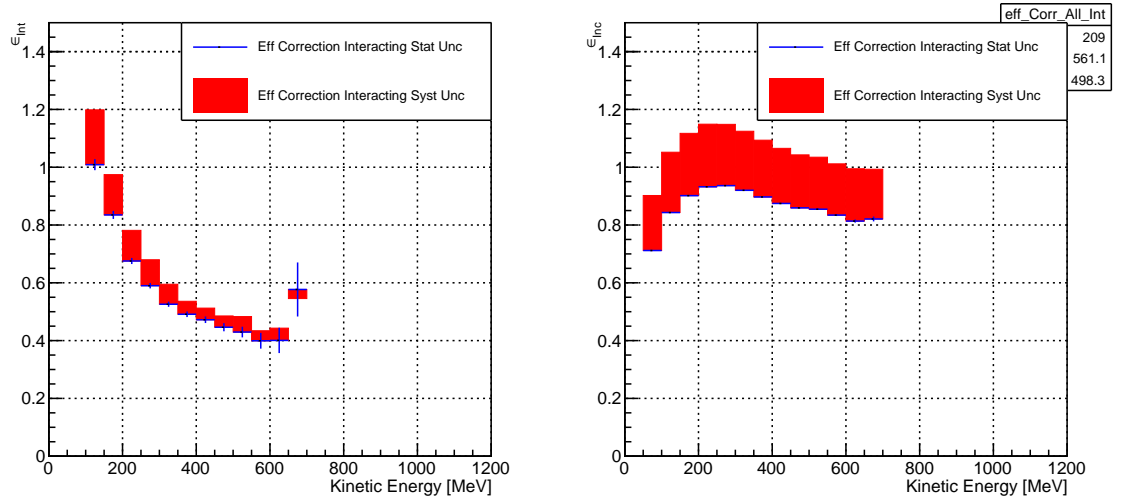


Figure 2.5: *Left*: Efficiency correction on the interacting histogram, statistical uncertainty in blue, systematic uncertainty in red. *Right*: Efficiency correction on the incident histogram, statistical uncertainty in blue, systematic uncertainty in red.



690 surement, the systematic uncertainty related to the beam composition and the sys-  
691 tematic uncertainty related to the efficiency correction.

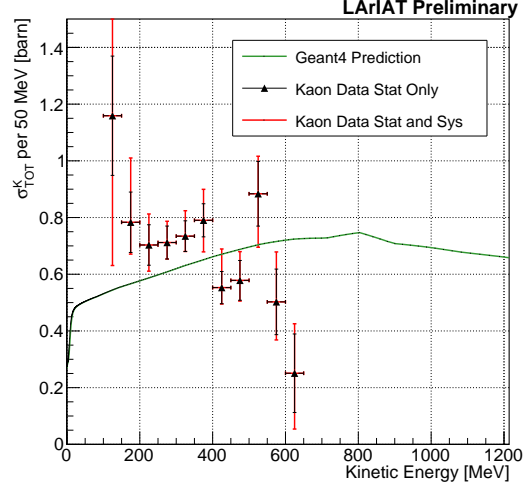


Figure 2.6: ( $K^+$ -Ar) total hadronic cross section for scattering angles greater than  $5^\circ$  measured in the 60A sample, statistical uncertainty in black and systematic uncertainty in red. The Geant4 prediction for the total hadronic cross section for angle scattering greater than  $5^\circ$  is displayed in green.

# Bibliography

- [1] PDG Tables for Liquid Argon. . Technical report.
- [2] Precision electroweak measurements on the  $z$  resonance. *Physics Reports*, 427(5):257 – 454, 2006.
- [3] K. Abe, J. Amey, C. Andreopoulos, M. Antonova, S. Aoki, A. Ariga, D. Autiero, S. Ban, M. Barbi, G. J. Barker, G. Barr, C. Barry, P. Bartet-Friburg, M. Batkiewicz, V. Berardi, S. Berkman, S. Bhadra, S. Bienstock, A. Blondel, S. Bolognesi, S. Bordoni, S. B. Boyd, D. Brailsford, A. Bravar, C. Bronner, M. Buizza Avanzini, R. G. Calland, T. Campbell, S. Cao, S. L. Cartwright, M. G. Catanesi, A. Cervera, C. Checchia, D. Cherdack, N. Chikuma, G. Christodoulou, A. Clifton, J. Coleman, G. Collazuol, D. Coploue, A. Cudd, A. Dabrowska, G. De Rosa, T. Dealtry, P. F. Denner, S. R. Dennis, C. Densham, D. Dewhurst, F. Di Lodovico, S. Di Luise, S. Dolan, O. Drapier, K. E. Duffy, J. Dumarchez, M. Dziewiecki, S. Emery-Schrenk, A. Ereditato, T. Feusels, A. J. Finch, G. A. Fiorentini, M. Friend, Y. Fujii, D. Fukuda, Y. Fukuda, V. Galymov, A. Garcia, C. Giganti, F. Gizzarelli, T. Golan, M. Gonin, D. R. Hadley, L. Haegel, M. D. Haigh, D. Hansen, J. Harada, M. Hartz, T. Hasegawa, N. C. Hastings, T. Hayashino, Y. Hayato, R. L. Helmer, A. Hillairet, T. Hiraki, A. Hiramoto, S. Hirota, M. Hogan, J. Holeczek, F. Hosomi, K. Huang, A. K. Ichikawa, M. Ikeda, J. Imber, J. Insler, R. A. Intonti, T. Ishida, T. Ishii, E. Iwai, K. Iwamoto, A. Izmaylov, B. Jamieson, M. Jiang, S. Johnson, P. Jonsson,

713 C. K. Jung, M. Kabirnezhad, A. C. Kaboth, T. Kajita, H. Kakuno, J. Kameda,  
 714 D. Karlen, T. Katori, E. Kearns, M. Khabibullin, A. Khotjantsev, H. Kim,  
 715 J. Kim, S. King, J. Kisiel, A. Knight, A. Knox, T. Kobayashi, L. Koch, T. Koga,  
 716 A. Konaka, K. Kondo, L. L. Kormos, A. Korzenev, Y. Koshio, K. Kowalik,  
 717 W. Kropp, Y. Kudenko, R. Kurjata, T. Kutter, J. Lagoda, I. Lamont, M. Lam-  
 718 oureux, E. Larkin, P. Lasorak, M. Laveder, M. Lawe, M. Licciardi, T. Lindner,  
 719 Z. J. Liptak, R. P. Litchfield, X. Li, A. Longhin, J. P. Lopez, T. Lou, L. Ludovici,  
 720 X. Lu, L. Magaletti, K. Mahn, M. Malek, S. Manly, A. D. Marino, J. F. Martin,  
 721 P. Martins, S. Martynenko, T. Maruyama, V. Matveev, K. Mavrokoridis, W. Y.  
 722 Ma, E. Mazzucato, M. McCarthy, N. McCauley, K. S. McFarland, C. McGrew,  
 723 A. Mefodiev, C. Metelko, M. Mezzetto, P. Mijakowski, A. Minamino, O. Mi-  
 724 neev, S. Mine, A. Missert, M. Miura, S. Moriyama, Th. A. Mueller, J. Myslik,  
 725 T. Nakadaira, M. Nakahata, K. G. Nakamura, K. Nakamura, K. D. Nakamura,  
 726 Y. Nakanishi, S. Nakayama, T. Nakaya, K. Nakayoshi, C. Nantais, C. Nielsen,  
 727 M. Nirkko, K. Nishikawa, Y. Nishimura, P. Novella, J. Nowak, H. M. O’Keeffe,  
 728 K. Okumura, T. Okusawa, W. Oryszczak, S. M. Oser, T. Ovsyannikova, R. A.  
 729 Owen, Y. Oyama, V. Palladino, J. L. Palomino, V. Paolone, N. D. Patel,  
 730 P. Paudyal, M. Pavin, D. Payne, J. D. Perkin, Y. Petrov, L. Pickard, L. Pick-  
 731 ering, E. S. Pinzon Guerra, C. Pistillo, B. Popov, M. Posiadala-Zezula, J.-M.  
 732 Poutissou, R. Poutissou, P. Przewlocki, B. Quilain, T. Radermacher, E. Radi-  
 733 cioni, P. N. Ratoff, M. Ravonel, M. A. Rayner, A. Redij, E. Reinherz-Aronis,  
 734 C. Riccio, P. A. Rodrigues, E. Rondio, B. Rossi, S. Roth, A. Rubbia, A. Rychter,  
 735 K. Sakashita, F. Sánchez, E. Scantamburlo, K. Scholberg, J. Schwehr, M. Scott,  
 736 Y. Seiya, T. Sekiguchi, H. Sekiya, D. Sgalaberna, R. Shah, A. Shaikhiev,  
 737 F. Shaker, D. Shaw, M. Shiozawa, T. Shirahige, S. Short, M. Smy, J. T.  
 738 Sobczyk, H. Sobel, M. Sorel, L. Southwell, J. Steinmann, T. Stewart, P. Stowell,  
 739 Y. Suda, S. Suvorov, A. Suzuki, S. Y. Suzuki, Y. Suzuki, R. Tacik, M. Tada,

740 A. Takeda, Y. Takeuchi, H. K. Tanaka, H. A. Tanaka, D. Terhorst, R. Terri,  
 741 T. Thakore, L. F. Thompson, S. Tobayama, W. Toki, T. Tomura, C. Tourama-  
 742 nis, T. Tsukamoto, M. Tzanov, Y. Uchida, M. Vagins, Z. Vallari, G. Vasseur,  
 743 T. Vladisavljevic, T. Wachala, C. W. Walter, D. Wark, M. O. Wascko, A. We-  
 744 ber, R. Wendell, R. J. Wilkes, M. J. Wilking, C. Wilkinson, J. R. Wilson, R. J.  
 745 Wilson, C. Wret, Y. Yamada, K. Yamamoto, M. Yamamoto, C. Yanagisawa,  
 746 T. Yano, S. Yen, N. Yershov, M. Yokoyama, K. Yoshida, T. Yuan, M. Yu, A. Za-  
 747 lewska, J. Zalipska, L. Zambelli, K. Zaremba, M. Ziembicki, E. D. Zimmerman,  
 748 M. Zito, and J. Żmuda. Combined analysis of neutrino and antineutrino oscil-  
 749 lations at t2k. *Phys. Rev. Lett.*, 118:151801, Apr 2017.

750 [4] K. Abe, Y. Haga, Y. Hayato, M. Ikeda, K. Iyogi, J. Kameda, Y. Kishimoto,  
 751 M. Miura, S. Moriyama, M. Nakahata, T. Nakajima, Y. Nakano, S. Nakayama,  
 752 A. Orii, H. Sekiya, M. Shiozawa, A. Takeda, H. Tanaka, T. Tomura, R. A. Wen-  
 753 dell, R. Akutsu, T. Irvine, T. Kajita, K. Kaneyuki, Y. Nishimura, E. Richard,  
 754 K. Okumura, L. Labarga, P. Fernandez, J. Gustafson, C. Kachulis, E. Kearns,  
 755 J. L. Raaf, J. L. Stone, L. R. Sulak, S. Berkman, C. M. Nantais, H. A.  
 756 Tanaka, S. Tobayama, M. Goldhaber, W. R. Kropp, S. Mine, P. Weatherly,  
 757 M. B. Smy, H. W. Sobel, V. Takhistov, K. S. Ganezer, B. L. Hartfiel, J. Hill,  
 758 N. Hong, J. Y. Kim, I. T. Lim, R. G. Park, A. Himmel, Z. Li, E. O’Sullivan,  
 759 K. Scholberg, C. W. Walter, T. Wongjirad, T. Ishizuka, S. Tasaka, J. S. Jang,  
 760 J. G. Learned, S. Matsuno, S. N. Smith, M. Friend, T. Hasegawa, T. Ishida,  
 761 T. Ishii, T. Kobayashi, T. Nakadaira, K. Nakamura, Y. Oyama, K. Sakashita,  
 762 T. Sekiguchi, T. Tsukamoto, A. T. Suzuki, Y. Takeuchi, T. Yano, S. V. Cao,  
 763 T. Hiraki, S. Hirota, K. Huang, T. Kikawa, A. Minamino, T. Nakaya, K. Suzuki,  
 764 Y. Fukuda, K. Choi, Y. Itow, T. Suzuki, P. Mijakowski, K. Frankiewicz, J. Hig-  
 765 night, J. Imber, C. K. Jung, X. Li, J. L. Palomino, M. J. Wilking, C. Yanag-  
 766 isawa, D. Fukuda, H. Ishino, T. Kayano, A. Kibayashi, Y. Koshio, T. Mori,

767 M. Sakuda, C. Xu, Y. Kuno, R. Tacik, S. B. Kim, H. Okazawa, Y. Choi,  
768 K. Nishijima, M. Koshihara, Y. Totsuka, Y. Suda, M. Yokoyama, C. Bronner,  
769 M. Hartz, K. Martens, Ll. Marti, Y. Suzuki, M. R. Vagins, J. F. Martin, A. Kon-  
770 aka, S. Chen, Y. Zhang, and R. J. Wilkes. Search for proton decay via  $p \rightarrow e^+ \pi^0$   
771 and  $p \rightarrow \mu^+ \pi^0$  in 0.31 megaton  $\cdot$  years exposure of the super-kamiokande water  
772 cherenkov detector. *Phys. Rev. D*, 95:012004, Jan 2017.

773 [5] R Acciarri, C Adams, J Asaadi, B Baller, T Bolton, C Bromberg, F Ca-  
774 vanna, E Church, D Edmunds, A Ereditato, S Farooq, B Fleming, H Greenlee,  
775 G Horton-Smith, C James, E Klein, K Lang, P Laurens, D McKee, R Mehdiyev,  
776 B Page, O Palamara, K Partyka, G Rameika, B Rebel, M Soderberg, J Spitz,  
777 A M Szelc, M Weber, M Wojcik, T Yang, and G P Zeller. A study of electron  
778 recombination using highly ionizing particles in the argoneut liquid argon tpc.  
779 *Journal of Instrumentation*, 8(08):P08005, 2013.

780 [6] R Acciarri, M Antonello, B Baibussinov, M Baldo-Ceolin, P Benetti,  
781 F Calaprice, E Calligarich, M Cambiaghi, N Canci, F Carbonara, F Cavanna,  
782 S Centro, A G Cocco, F Di Pompeo, G Fiorillo, C Galbiati, V Gallo, L Grandi,  
783 G Meng, I Modena, C Montanari, O Palamara, L Pandola, G B Piano Mortari,  
784 F Pietropaolo, G L Raselli, M Roncadelli, M Rossella, C Rubbia, E Segreto,  
785 A M Szelc, S Ventura, and C Vignoli. Effects of nitrogen contamination in  
786 liquid argon. *Journal of Instrumentation*, 5(06):P06003, 2010.

787 [7] R. Acciarri et al. Demonstration and Comparison of Operation of Photomulti-  
788 plier Tubes at Liquid Argon Temperature. *JINST*, 7:P01016, 2012.

789 [8] R. Acciarri et al. Design and Construction of the MicroBooNE Detector. *JINST*,  
790 12(02):P02017, 2017.

- [9] R. Acciarri et al. First Observation of Low Energy Electron Neutrinos in a Liquid Argon Time Projection Chamber. *Phys. Rev.*, D95(7):072005, 2017. [Phys. Rev.D95,072005(2017)].
- [10] M Adamowski, B Carls, E Dvorak, A Hahn, W Jaskierny, C Johnson, H Jostlein, C Kendziora, S Lockwitz, B Pahlka, R Plunkett, S Pordes, B Rebel, R Schmitt, M Stancari, T Tope, E Voirin, and T Yang. The liquid argon purity demonstrator. *Journal of Instrumentation*, 9(07):P07005, 2014.
- [11] C. Adams et al. The Long-Baseline Neutrino Experiment: Exploring Fundamental Symmetries of the Universe. 2013.
- [12] P. Adamson, L. Aliaga, D. Ambrose, N. Anfimov, A. Antoshkin, E. Arrieta-Diaz, K. Augsten, A. Aurisano, C. Backhouse, M. Baird, B. A. Bambah, K. Bays, B. Behera, S. Bending, R. Bernstein, V. Bhatnagar, B. Bhuyan, J. Bian, T. Blackburn, A. Bolshakova, C. Bromberg, J. Brown, G. Brunetti, N. Buchanan, A. Butkevich, V. Bychkov, M. Campbell, E. Catano-Mur, S. Childress, B. C. Choudhary, B. Chowdhury, T. E. Coan, J. A. B. Coelho, M. Colo, J. Cooper, L. Corwin, L. Cremonesi, D. Cronin-Hennessy, G. S. Davies, J. P. Davies, P. F. Derwent, R. Dharmapalan, P. Ding, Z. Djurcic, E. C. Dukes, H. Duyang, S. Edayath, R. Ehrlich, G. J. Feldman, M. J. Frank, M. Gabrielyan, H. R. Gallagher, S. Germani, T. Ghosh, A. Giri, R. A. Gomes, M. C. Goodman, V. Grichine, R. Group, D. Grover, B. Guo, A. Habig, J. Hartnell, R. Hatcher, A. Hatzikoutelis, K. Heller, A. Himmel, A. Holin, J. Hylen, F. Jediny, M. Judah, G. K. Kafka, D. Kalra, S. M. S. Kasahara, S. Kasetti, R. Keloth, L. Kolupaeva, S. Kotelnikov, I. Kourbanis, A. Kreymer, A. Kumar, S. Kurbanov, K. Lang, W. M. Lee, S. Lin, J. Liu, M. Lokajicek, J. Lozier, S. Luchuk, K. Maan, S. Magill, W. A. Mann, M. L. Marshak, K. Matera, V. Matveev, D. P. Méndez, M. D. Messier, H. Meyer, T. Miao, W. H. Miller, S. R. Mishra, R. Mohanta, A. Moren,

817 L. Mualem, M. Muether, S. Mufson, R. Murphy, J. Musser, J. K. Nelson,  
 818 R. Nichol, E. Niner, A. Norman, T. Nosek, Y. Oksuzian, A. Olshevskiy, T. Ol-  
 819 son, J. Paley, P. Pandey, R. B. Patterson, G. Pawloski, D. Pershey, O. Petrova,  
 820 R. Petti, S. Phan-Budd, R. K. Plunkett, R. Poling, B. Potukuchi, C. Principato,  
 821 F. Psihas, A. Radovic, R. A. Rameika, B. Rebel, B. Reed, D. Rocco, P. Rojas,  
 822 V. Ryabov, K. Sachdev, P. Sail, O. Samoylov, M. C. Sanchez, R. Schroeter,  
 823 J. Sepulveda-Quiroz, P. Shanahan, A. Sheshukov, J. Singh, J. Singh, P. Singh,  
 824 V. Singh, J. Smolik, N. Solomey, E. Song, A. Sousa, K. Soustruznik, M. Strait,  
 825 L. Suter, R. L. Talaga, M. C. Tamsett, P. Tas, R. B. Thayyullathil, J. Thomas,  
 826 X. Tian, S. C. Tognini, J. Tripathi, A. Tsaris, J. Urheim, P. Vahle, J. Vasel,  
 827 L. Vinton, A. Vold, T. Vrba, B. Wang, M. Wetstein, D. Whittington, S. G. Wo-  
 828 jcicki, J. Wolcott, N. Yadav, S. Yang, J. Zalesak, B. Zamorano, and R. Zwaska.  
 829 Constraints on oscillation parameters from  $\nu_e$  appearance and  $\nu_\mu$  disappearance  
 830 in nova. *Phys. Rev. Lett.*, 118:231801, Jun 2017.

831 [13] Alan Agresti. *Categorical Data Analysis*. Wiley Series in Probability and Statis-  
 832 tics. Wiley, 2013.

833 [14] A. Aguilar-Arevalo et al. Evidence for neutrino oscillations from the observation  
 834 of anti-neutrino(electron) appearance in a anti-neutrino(muon) beam. *Phys.*  
 835 *Rev.*, D64:112007, 2001.

836 [15] A. A. Aguilar-Arevalo et al. Improved Search for  $\bar{\nu}_\mu \rightarrow \bar{\nu}_e$  Oscillations in the  
 837 MiniBooNE Experiment. *Phys. Rev. Lett.*, 110:161801, 2013.

838 [16] S. Amoruso et al. Study of electron recombination in liquid argon with the  
 839 ICARUS TPC. *Nucl. Instrum. Meth.*, A523:275–286, 2004.

840 [17] C. Anderson et al. The ArgoNeuT Detector in the NuMI Low-Energy beam  
 841 line at Fermilab. *JINST*, 7:P10019, 2012.

- [18] C. Andreopoulos et al. The GENIE Neutrino Monte Carlo Generator. *Nucl. Instrum. Meth.*, A614:87–104, 2010.
- [19] Timofei Bolshakov Andrey Petrov. Java synoptic toolkit. Technical report, Sept 2010.
- [20] M. Antonello, B. Baibussinov, P. Benetti, E. Calligarich, N. Canci, S. Centro, A. Cesana, K. Cieslik, D. B. Cline, A. G. Cocco, A. Dabrowska, D. Dequal, A. Dermenev, R. Dolfini, C. Farnese, A. Fava, A. Ferrari, G. Fiorillo, D. Gibin, S. Gninenko, A. Guglielmi, M. Haranczyk, J. Holeczek, A. Ivashkin, J. Kisiel, I. Kochanek, J. Lagoda, S. Mania, A. Menegolli, G. Meng, C. Montanari, S. Otwinowski, A. Piazzoli, P. Picchi, F. Pietropaolo, P. Plonski, A. Rappoldi, G. L. Raselli, M. Rossella, C. Rubbia, P. Sala, A. Scaramelli, E. Segreto, F. Sergiampietri, D. Stefan, J. Stepaniak, R. Sulej, M. Szarska, M. Ter-rani, F. Varanini, S. Ventura, C. Vignoli, H. Wang, X. Yang, A. Zalewska, and K. Zaremba. Precise 3d track reconstruction algorithm for the ICARUS t600 liquid argon time projection chamber detector. *Advances in High Energy Physics*, 2013:1–16, 2013.
- [21] M. Antonello et al. A Proposal for a Three Detector Short-Baseline Neutrino Oscillation Program in the Fermilab Booster Neutrino Beam. 2015.
- [22] D. Ashery, I. Navon, G. Azuelos, H. K. Walter, H. J. Pfeiffer, and F. W. Schlepütz. True absorption and scattering of pions on nuclei. *Phys. Rev. C*, 23:2173–2185, May 1981.
- [23] C. Athanassopoulos et al. Evidence for  $\nu(\mu) \rightarrow \nu(e)$  neutrino oscillations from LSND. *Phys. Rev. Lett.*, 81:1774–1777, 1998.



- [24] Borut Bajc, Junji Hisano, Takumi Kuwahara, and Yuji Omura. Threshold corrections to dimension-six proton decay operators in non-minimal {SUSY} su(5) {GUTs}. *Nuclear Physics B*, 910:1 – 22, 2016.
- [25] B. Baller. Trajcluster user guide. Technical report, apr 2016.
- [26] Gary Barker. Neutrino event reconstruction in a liquid argon TPC. *Journal of Physics: Conference Series*, 308:012015, jul 2011.
- [27] BASF Corp. 100 Park Avenue, Florham Park, NJ 07932 USA.
- [28] R. Becker-Szendy, C. B. Bratton, D. R. Cady, D. Casper, R. Claus, M. Crouch, S. T. Dye, W. Gajewski, M. Goldhaber, T. J. Haines, P. G. Halverson, T. W. Jones, D. Kielczewska, W. R. Kropp, J. G. Learned, J. M. LoSecco, C. McGrew, S. Matsuno, J. Matthews, M. S. Mudah, L. Price, F. Reines, J. Schultz, D. Sinclair, H. W. Sobel, J. L. Stone, L. R. Sulak, R. Svoboda, G. Thornton, and J. C. van der Velde. Search for proton decay into  $e^+ + \pi^0$  in the imb-3 detector. *Phys. Rev. D*, 42:2974–2976, Nov 1990.
- [29] J B Birks. Scintillations from organic crystals: Specific fluorescence and relative response to different radiations. *Proceedings of the Physical Society. Section A*, 64(10):874, 1951.
- [30] A. Bodek and J. L. Ritchie. Further studies of fermi-motion effects in lepton scattering from nuclear targets. *Phys. Rev. D*, 24:1400–1402, Sep 1981.
- [31] Mark G. Boulay and A. Hime. Direct WIMP detection using scintillation time discrimination in liquid argon. 2004.
- [32] D. V. Bugg, R. S. Gilmore, K. M. Knight, D. C. Salter, G. H. Stafford, E. J. N. Wilson, J. D. Davies, J. D. Dowell, P. M. Hattersley, R. J. Homer, A. W. O’dell,

888 A. A. Carter, R. J. Tapper, and K. F. Riley. Kaon-nucleon total cross sections  
889 from 0.6 to 2.65 gev/ *c. Phys. Rev.*, 168:1466–1475, Apr 1968.

890 [33] W. M. Burton and B. A. Powell. Fluorescence of tetraphenyl-butadiene in the  
891 vacuum ultraviolet. *Applied Optics*, 12(1):87, jan 1973.

892 [34] CAEN. Caen v1495 data sheet. Technical report, jan 2018.

893 [35] CAEN. Caen v1740 data sheet. Technical report, jan 2018.

894 [36] A. S. Carroll, I. H. Chiang, C. B. Dover, T. F. Kycia, K. K. Li, P. O. Mazur,  
895 D. N. Michael, P. M. Mockett, D. C. Rahm, and R. Rubinstein. Pion-nucleus  
896 total cross sections in the (3,3) resonance region. *Phys. Rev. C*, 14:635–638,  
897 Aug 1976.

898 [37] D. Casper. The nuance neutrino physics simulation, and the future. *Nuclear*  
899 *Physics B - Proceedings Supplements*, 112(1-3):161–170, nov 2002.

900 [38] A. Cervera, A. Donini, M.B. Gavela, J.J. Gomez Cádenas, P. Hernández,  
901 O. Mena, and S. Rigolin. Golden measurements at a neutrino factory. *Nu-*  
902 *clear Physics B*, 579(1-2):17–55, jul 2000.

903 [39] E. Church. LArSoft: A Software Package for Liquid Argon Time Projection  
904 Drift Chambers. 2013.

905 [40] ATLAS Collaboration. Observation of a new particle in the search for the  
906 standard model higgs boson with the ATLAS detector at the LHC. *Physics*  
907 *Letters B*, 716(1):1–29, sep 2012.

908 [41] CMS Collaboration. Observation of a new boson at a mass of 125 gev with the  
909 cms experiment at the lhc. *Physics Letters B*, 716(1):30 – 61, 2012.

910 [42] The LArIAT Collaboration. The liquid argon in a testbeam (lariat) experiment.  
911 Technical report, In Preparation 2018.

- [43] Stefano Dell’Oro, Simone Marcocci, Matteo Viel, and Francesco Vissani. Neutrinoless double beta decay: 2015 review. *Advances in High Energy Physics*, 2016:1–37, 2016.
- [44] S.E. Derenzo, A.R. Kirschbaum, P.H. Eberhard, R.R. Ross, and F.T. Solmitz. Test of a liquid argon chamber with 20 m rms resolution. *Nuclear Instruments and Methods*, 122:319 – 327, 1974.
- [45] Savas Dimopoulos, Stuart Raby, and Frank Wilczek. Proton Decay in Supersymmetric Models. *Phys. Lett.*, B112:133, 1982.
- [46] D. Drakoulakos et al. Proposal to perform a high-statistics neutrino scattering experiment using a fine-grained detector in the NuMI beam. 2004.
- [47] A Ereditato, C C Hsu, S Janos, I Kreslo, M Messina, C Rudolf von Rohr, B Rossi, T Strauss, M S Weber, and M Zeller. Design and operation of argontube: a 5 m long drift liquid argon tpc. *Journal of Instrumentation*, 8(07):P07002, 2013.
- [48] Torleif Ericson and Wolfram Weise. *Pions and Nuclei (The International Series of Monographs on Physics)*. Oxford University Press, 1988.
- [49] A.A. Aguilar-Arevalo et al. The miniboone detector. *Nuclear Instruments and Methods in Physics Research Section A: Accelerators, Spectrometers, Detectors and Associated Equipment*, 599(1):28 – 46, 2009.
- [50] Antonio Bueno et al. Nucleon decay searches with large liquid argon TPC detectors at shallow depths: atmospheric neutrinos and cosmogenic backgrounds. *Journal of High Energy Physics*, 2007(04):041–041, apr 2007.
- [51] A.S. Clough et al. Pion-nucleus total cross sections from 88 to 860 MeV. *Nuclear Physics B*, 76(1):15–28, jul 1974.

- [52] B.W. Allardyce et al. Pion reaction cross sections and nuclear sizes. *Nuclear Physics A*, 209(1):1 – 51, 1973.
- [53] C Athanassopoulos et al. The liquid scintillator neutrino detector and LAMPF neutrino source. *Nuclear Instruments and Methods in Physics Research Section A: Accelerators, Spectrometers, Detectors and Associated Equipment*, 388(1-2):149–172, mar 1997.
- [54] F. Binon et al. Scattering of negative pions on carbon. *Nuclear Physics B*, 17(1):168 – 188, 1970.
- [55] L. Aliaga et al. Minerva neutrino detector response measured with test beam data. *Nuclear Instruments and Methods in Physics Research Section A: Accelerators, Spectrometers, Detectors and Associated Equipment*, 789:28 – 42, 2015.
- [56] M Adamowski et al. The liquid argon purity demonstrator. *Journal of Instrumentation*, 9(07):P07005, 2014.
- [57] P. Vilain et al. Coherent single charged pion production by neutrinos. *Physics Letters B*, 313(1-2):267–275, aug 1993.
- [58] R. Acciarri et al. Convolutional neural networks applied to neutrino events in a liquid argon time projection chamber. *Journal of Instrumentation*, 12(03):P03011, 2017.
- [59] R. Acciarri et al. Design and construction of the MicroBooNE detector. *Journal of Instrumentation*, 12(02):P02017–P02017, feb 2017.
- [60] C. E. Aalseth et al. DarkSide-20k: A 20 tonne two-phase LAr TPC for direct dark matter detection at LNGS. *The European Physical Journal Plus*, 133(3), mar 2018.

- [61] H Fenker. Standard beam pwc for fermilab. Technical report, Fermi National Accelerator Lab., Batavia, IL (USA), 1983.
- [62] H Fesbach. Theoretical nuclear physics: Nuclear reactions. 1992.
- [63] J. A. Formaggio and G. P. Zeller. From ev to eev: Neutrino cross sections across energy scales. *Rev. Mod. Phys.*, 84:1307–1341, Sep 2012.
- [64] E. Friedman et al. K+ nucleus reaction and total cross-sections: New analysis of transmission experiments. *Phys. Rev.*, C55:1304–1311, 1997.
- [65] V.M. Gehman, S.R. Seibert, K. Rielage, A. Hime, Y. Sun, D.-M. Mei, J. Maassen, and D. Moore. Fluorescence efficiency and visible re-emission spectrum of tetraphenyl butadiene films at extreme ultraviolet wavelengths. *Nuclear Instruments and Methods in Physics Research Section A: Accelerators, Spectrometers, Detectors and Associated Equipment*, 654(1):116 – 121, 2011.
- [66] H. Geiger and E. Marsden. On a diffuse reflection of the formula-particles. *Proceedings of the Royal Society A: Mathematical, Physical and Engineering Sciences*, 82(557):495–500, jul 1909.
- [67] Howard Georgi and S. L. Glashow. Unity of all elementary-particle forces. *Phys. Rev. Lett.*, 32:438–441, Feb 1974.
- [68] D.Y. Wong (editor) G.L. Shaw (Editor). *Pion-nucleon Scattering*. John Wiley & Sons Inc, 1969.
- [69] Glassman High Voltage, Inc., Precision Regulated High Voltage DC Power Supply.
- [70] D S Gorbunov. Sterile neutrinos and their role in particle physics and cosmology. *Physics-Uspekhi*, 57(5):503, 2014.

- [71] C. Green, J. Kowalkowski, M. Paterno, M. Fischler, L. Garren, and Q. Lu. The Art Framework. *J. Phys. Conf. Ser.*, 396:022020, 2012.
- [72] S. Hansen, D. Jensen, G. Savage, E. Skup, and A. Soha. Fermilab test beam multi-wire proportional chamber tracking system upgrade. June 2014. International Conference on Technology and Instrumentation in Particle Physics (TIPP 2014).
- [73] J. Harada. Non-maximal  $\theta_{23}$  , large  $\theta_{13}$  and tri-bimaximal  $\theta_{12}$  via quark-lepton complementarity at next-to-leading order. *EPL (Europhysics Letters)*, 103(2):21001, 2013.
- [74] Peter W. Higgs. Broken symmetries and the masses of gauge bosons. *Physical Review Letters*, 13(16):508–509, oct 1964.
- [75] P.W. Higgs. Broken symmetries, massless particles and gauge fields. *Physics Letters*, 12(2):132–133, sep 1964.
- [76] H J Hilke. Time projection chambers. *Reports on Progress in Physics*, 73(11):116201, 2010.
- [77] N. Ishida, M. Chen, T. Doke, K. Hasuike, A. Hitachi, M. Gaudreau, M. Kase, Y. Kawada, J. Kikuchi, T. Komiyama, K. Kuwahara, K. Masuda, H. Okada, Y.H. Qu, M. Suzuki, and T. Takahashi. Attenuation length measurements of scintillation light in liquid rare gases and their mixtures using an improved reflection suppresser. *Nuclear Instruments and Methods in Physics Research Section A: Accelerators, Spectrometers, Detectors and Associated Equipment*, 384(2-3):380–386, jan 1997.
- [78] G. Pulliam J. Asaadi, E. Gramellini. Determination of the electron lifetime in lariat. Technical report, August 2017.

- 1007 [79] George Jaffé. Zur theorie der ionisation in kolonnen. *Annalen der Physik*,  
1008 347(12):303–344, 1913.
- 1009 [80] C. Jarlskog. A basis independent formulation of the connection between quark  
1010 mass matrices, CP violation and experiment. *Zeitschrift für Physik C Particles  
1011 and Fields*, 29(3):491–497, sep 1985.
- 1012 [81] B J P Jones, C S Chiu, J M Conrad, C M Ignarra, T Katori, and M Toups. A  
1013 measurement of the absorption of liquid argon scintillation light by dissolved ni-  
1014 trogen at the part-per-million level. *Journal of Instrumentation*, 8(07):P07011,  
1015 2013.
- 1016 [82] Benjamin J. P. Jones. *Sterile Neutrinos in Cold Climates*. PhD thesis, MIT,  
1017 2015.
- 1018 [83] Cezary Juszczak, Jarosław A. Nowak, and Jan T. Sobczyk. Simulations from  
1019 a new neutrino event generator. *Nuclear Physics B - Proceedings Supplements*,  
1020 159:211–216, sep 2006.
- 1021 [84] D. I. Kazakov. Beyond the standard model: In search of supersymmetry. In  
1022 *2000 European School of high-energy physics, Caramulo, Portugal, 20 Aug-2  
1023 Sep 2000: Proceedings*, pages 125–199, 2000.
- 1024 [85] Dae-Gyu Lee, R. N. Mohapatra, M. K. Parida, and Merostar Rani. Predic-  
1025 tions for the proton lifetime in minimal nonsupersymmetric  $so(10)$  models: An  
1026 update. *Phys. Rev. D*, 51:229–235, Jan 1995.
- 1027 [86] M A Leigui de Oliveira. Expression of Interest for a Full-Scale Detector Engi-  
1028 neering Test and Test Beam Calibration of a Single-Phase LAr TPC. Technical  
1029 Report CERN-SPSC-2014-027. SPSC-EOI-011, CERN, Geneva, Oct 2014.

- 1030 [87] W. H. Lippincott, K. J. Coakley, D. Gastler, A. Hime, E. Kearns, D. N. McK-  
1031 insey, J. A. Nikkel, and L. C. Stonehill. Scintillation time dependence and pulse  
1032 shape discrimination in liquid argon. *Phys. Rev. C*, 78:035801, Sep 2008.
- 1033 [88] Jorge L. Lopez and Dimitri V. Nanopoulos. Flipped SU(5): Origins and re-  
1034 cent developments. In *15th Johns Hopkins Workshop on Current Problems*  
1035 *in Particle Theory: Particle Physics from Underground to Heaven Baltimore,*  
1036 *Maryland, August 26-28, 1991*, pages 277–297, 1991.
- 1037 [89] Vincent Lucas and Stuart Raby. Nucleon decay in a realistic so(10) susy gut.  
1038 *Phys. Rev. D*, 55:6986–7009, Jun 1997.
- 1039 [90] Ettore Majorana. Teoria simmetrica dell’elettrone e del positrone. *Il Nuovo*  
1040 *Cimento*, 14(4):171–184, apr 1937.
- 1041 [91] Hisakazu Minakata and Alexei Yu. Smirnov. Neutrino mixing and quark-lepton  
1042 complementarity. *Phys. Rev. D*, 70:073009, Oct 2004.
- 1043 [92] M. Mooney. The microboone experiment and the impact of space charge effects.  
1044 2015.
- 1045 [93] E. Morikawa, R. Reininger, P. Görtler, V. Saile, and P. Laporte. Argon, kryp-  
1046 ton, and xenon excimer luminescence: From the dilute gas to the condensed  
1047 phase. *The Journal of Chemical Physics*, 91(3):1469–1477, aug 1989.
- 1048 [94] FM Newcomer, S Tedja, R Van Berg, J Van der Spiegel, and HH Williams.  
1049 A fast, low power, amplifier-shaper-discriminator for high rate straw tracking  
1050 systems. *IEEE Transactions on Nuclear Science*, 40(4):630–636, 1993.
- 1051 [95] Emmy Noether. Invariant variation problems. *Transport Theory and Statistical*  
1052 *Physics*, 1(3):186–207, jan 1971.



- [96] I. Nutini. Study of charged particles interaction processes on ar in the 0.2 - 2.0 GeV energy range through combined information from ionization free charge and scintillation light. Technical report, jan 2015.
- [97] D. R. Nygren. The time projection chamber: A new  $4\pi$  detector for charged particles. Technical report, 1974.
- [98] L. Onsager. Initial recombination of ions. *Phys. Rev.*, 54:554–557, Oct 1938.
- [99] S. Pascoli, S.T. Petcov, and A. Riotto. Leptogenesis and low energy cp-violation in neutrino physics. *Nuclear Physics B*, 774(1):1 – 52, 2007.
- [100] C. Patrignani et al. Review of Particle Physics. *Chin. Phys.*, C40(10):100001, 2016.
- [101] B. Pontecorvo. Neutrino Experiments and the Problem of Conservation of Leptonic Charge. *Sov. Phys. JETP*, 26:984–988, 1968. [*Zh. Eksp. Teor. Fiz.*53,1717(1967)].
- [102] T. Yang R. Acciarri. Investigation of the non-uniformity observed in the wire response to charge in lariat run 1. Technical report, February 2017.
- [103] T. Yang R. Acciarri, M. Stancari. Determination of the electron lifetime in lariat. Technical report, March 2016.
- [104] Martti Raidal. Relation between the neutrino and quark mixing angles and grand unification. *Phys. Rev. Lett.*, 93:161801, Oct 2004.
- [105] Steve Ritz et al. Building for Discovery: Strategic Plan for U.S. Particle Physics in the Global Context. 2014.
- [106] C. Rubbia. The Liquid Argon Time Projection Chamber: A New Concept for Neutrino Detectors. 1977.

- 1076 [107] L.M. Saunders. Electromagnetic production of pions from nuclei. *Nucl. Phys.*,  
1077 *B7: 293-310(1968)*.
- 1078 [108] Qaisar Shafi and Zurab Tavartkiladze. Neutrino democracy, fermion mass hier-  
1079 archies, and proton decay from 5d su(5). *Phys. Rev. D*, 67:075007, Apr 2003.
- 1080 [109] Sigma-Aldrich, P.O. Box 14508, St. Louis, MO 63178 USA.
- 1081 [110] R. K. Teague and C. J. Pings. Refractive index and the lorentz-lorenz function  
1082 for gaseous and liquid argon, including a study of the coexistence curve near the  
1083 critical state. *The Journal of Chemical Physics*, 48(11):4973–4984, jun 1968.
- 1084 [111] J. Thomas and D. A. Imel. Recombination of electron-ion pairs in liquid argon  
1085 and liquid xenon. *Phys. Rev. A*, 36:614–616, Jul 1987.
- 1086 [112] D.R.O. Morrison N. Rivoire V. Flaminio, W.G. Moorhead. Compilation of  
1087 Cross Sections I:  $\pi^+$  and  $\pi^-$  Induced Reactions. *CERN-HERA*, pages 83–01,  
1088 1983.
- 1089 [113] D.R.O. Morrison N. Rivoire V. Flaminio, W.G. Moorhead. Compilation of  
1090 Cross Sections II:  $K^+$  and  $K^-$  Induced Reactions. *CERN-HERA*, pages 83–02,  
1091 1983.
- 1092 [114] W. Walkowiak. Drift velocity of free electrons in liquid argon. *Nuclear Instru-*  
1093 *ments and Methods in Physics Research Section A: Accelerators, Spectrometers,*  
1094 *Detectors and Associated Equipment*, 449(1-2):288–294, jul 2000.
- 1095 [115] Hermann Weyl. Gravitation and the electron. *Proceedings of the National*  
1096 *Academy of Sciences of the United States of America*, 15(4):323–334, 1929.
- 1097 [116] Colin et al Wilkin. A comparison of  $\pi^+$  and  $\pi^-$  total cross-sections of light  
1098 nuclei near the 3-3 resonance. *Nucl. Phys.*, B62:61–85, 1973.

- 1099 [117] D. H. Wright and M. H. Kelsey. The Geant4 Bertini Cascade. *Nucl. Instrum.*  
1100 *Meth.*, A804:175–188, 2015.
- 1101 [118] C. S. Wu, E. Ambler, R. W. Hayward, D. D. Hoppes, and R. P. Hudson.  
1102 Experimental test of parity conservation in beta decay. *Phys. Rev.*, 105:1413–  
1103 1415, Feb 1957.
- 1104 [119] N Yahlali, L M P Fernandes, K Gonzlez, A N C Garcia, and A Soriano. Imaging  
1105 with sipms in noble-gas detectors. *Journal of Instrumentation*, 8(01):C01003,  
1106 2013.
- 1107 [120] T. Yanagida. Horizontal symmetry and masses of neutrinos. *Progress of Theo-*  
1108 *retical Physics*, 64(3):1103–1105, sep 1980.